# Solutions For Transients in Arbitrarily Branching Cables: IV. Nonuniform Electrical Parameters

Guy Major and Jonathan D. Evans
University Laboratory of Physiology, Oxford, OX1 3PT, United Kingdom

ABSTRACT Solutions for transients in arbitrarily branching passive cable neurone models with a soma are extended to models with nonuniform electrical parameters and multiple dendritic shunts. The response to an injected current can again be represented as an infinite series of exponentially decaying components with system time constants obtained from the roots of a recursive transcendental equation. The reciprocity relations and global parameter dependencies are the same as for uniform models. Infinitely many "raw" electro-morphological models map onto a given "core" electrotonic model; local as well as global raw parameter trade-offs are now possible. The solutions are illustrated by means of biologically relevant examples: (i) the effects of nonuniform electrical parameters in a two-cylinder + soma cortical pyramidal cell model, (ii) the errors that can occur when uniformity is incorrectly assumed in a single cylinder model, (iii) nonsumming interactions between cells and electrodes that can dramatically increase the duration of the effective capacitative electrode artefact, and (iv) shunting inhibition and double impalements in a hippocampal CA1 pyramidal cell "cartoon" representation. These solutions should complement compartmental modelling techniques.

## LIST OF SYMBOLS*

| | |
|---|---|
| $A_n$ | $n$th amplitude component [mV] |
| $A_{n_{er}}$ | $A_n$ between segments $e$ and $r$ or vice-versa (specify $Z_e$, $X_r$), [mV] (Eq. 4) |
| $\tilde{A}_s$ | constant in $\tilde{G}_r(X_r, Z_e, p)$ at soma (Eq. 23) |
| $\tilde{B}_c$ | constant in $\tilde{G}_r(X_r, Z_e, p)$ for "mainline" segment $c$ (Eq. 24) |
| $c_s$ | lumped soma capacitance (= $\pi d_s^2 C_m$), [pF] |
| $C_m$ | global (default) cell specific membrane capacitance [$\mu$Fcm$^{-2}$]† |
| $d_s$ | soma diameter [$\mu$m]† |
| $dtrs_p$ | the set of daughter segments of segment $p$ |
| $E_n$ | position-independent "Electrical" part of $A_n$ [mV], (Eq. 13) |
| $g_s$ | soma conductance, including shunt (= $g_{shunt} + g_{sm}$), [nS] |
| $g_{shunt}$ | = $g_{shunt_0}$, somatic shunt conductance [nS]†§ |
| $g_{sm}$ | soma *membrane* conductance (= $\pi d_s^2/R_m$), [nS]§ |
| $G_r(X_r, Z_e, t)$ | voltage response at $X_r$ to unit point charge at $Z_e$ [mV], (Appendix 1) |
| $\tilde{G}_r(X_r, Z_e, p)$ | Laplace transform of $G_r(X_r, Z_e, t)$ with respect to $p$ |
| $G_s(Z_e, t)$ | voltage response at soma to unit point charge at $Z_e$ [mV] (Appendix 1) |
| $\tilde{G}_s(Z_e, p)$ | Laplace transform of $G_s(Z_e, t)$ with respect to $p$ |
| $p$ | complex Laplace transform variable [*dimensionless*] |
| $q$ | $(1 + \tau_m p)^{1/2}$ [*dimensionless*], (Appendices) |
| $q_j$ | $(1 + \tau_m p)^{1/2}$ [*dimensionless*], (Appendices) |
| $R_i$ | global (default) cell axial cytoplasmic resistivity [$\Omega$cm]† |
| $R_m$ | global (default) cell specific membrane resistivity [$\Omega$cm$^2$]† |
| *segs* | the set of all segment indices $j$ |
| *stems* | the set of indices of segments *st* originating from soma (i.e. *stem segments*) |
| $t$ | time [ms] |
| $t_{1090}$ | 10–90% rise time [ms] |
| $V_j(X_j, Z_e, t)$ | transmembrane voltage with dimensionless space parameters [mV] |
| $V_s(t)$ | $V_j(t)$ at soma [mV] |
| $x_j$ | physical distance from proximal end of segment $j$ [$\mu$m] |
| $X_j$ | electrotonic distance from proximal end of segment $j$ (= $x_j/\lambda_j$), [*dimensionless*] |
| $z_e$ | physical distance of excitation site from proximal end of segment $e$ [$\mu$m] |
| $Z_e$ | electrotonic distance of input site from proximal end of seg. $e$ [*dimensionless*] |

## GREEK SYMBOLS

| | |
|---|---|
| $\alpha^2$ | global (cell) separation constant (Eqs. 4, 6, 12) |
| $\alpha_j^2$ | local (segment) separation constant (Eqs. 4 and 6) |
| $\alpha_n$ | $n$th global eigenvalue of boundary problem (satisfies Eq. 11) |
| $\alpha_{jn}$ | $n$th segment $j$ eigenvalue (= $(\tau_{m_j}/\tau_n - 1)^{1/2}$) |
| $\epsilon$ | somatic shunt parameter $\tau_s/\tau_m$ [*dimensionless*] |
| $\kappa_{jn}$ | $n$th voltage continuity normalisation factor of segment $j$ (Eq. 8) |
| $\tilde{\kappa}_j$ | continuity factor in $\tilde{G}_r$ for segment $j$ (Eq. 22) |
| $\mu_j$ | branching constant of segment $j$; depends on $\alpha_j$ (Eq. 9) |
| $\mu_{jn}$ | $\mu_j$ when $\alpha_j = \alpha_{jn}$ |
| $\tilde{\mu}_j$ | branching constant in segment $j$ for $\tilde{G}_r$; depends on $q_j$ (Eq. 20) |
| $\nu_{jn}$ | term from segment $j$ in denominator of amplitude (Eq. 14) |
| $\psi_{jn}$ | spatial eigenfunction in segment $j$ [*dimensionless*], (Eq. 5) |
| $\tau_m$ | global (default) membrane time constant (= $R_m C_m$ = $c_s/g_{sm}$), [ms]§ |
| $\tau_n$ | $n$th equalising time constant [*ms*], (Eqs. 4 and 6) |

*Received for publication 8 September 1993 and in final form 21 December 1993.*

Address reprint requests to Guy Major, University Laboratory of Physiology, Parks Rd., Oxford OX1 3PT, United Kingdom. Tel.: 011-44-865-272507; Fax: 011-44-865-272469; email gm @ physiol.ox.ac.uk.



0006-3495/94/03/615/20 $2.00

$\tau_s$ effective time constant of soma with shunt included ($= c_s/g_s$), [ms]

$\tau_{sy_n}$ $n$th synaptic time constant for multi-exponential current input [ms]

* Units and relevant equation numbers in square brackets and parentheses, respectively.

† Raw electro-morphological parameters.

§ Core electrotonic parameters (see Table 2 also).

## INTRODUCTION

In the first paper of this series (Major et al., 1993a), referred to as "Paper I" below, a separation of variables solution was derived for voltage transients in a passive cable model of an arbitrarily branching neurone with a soma plus shunt. In the next paper (Major et al., 1993b), referred to as "Paper II" below, analogous solutions were derived for models under voltage clamp. In the third paper (Major, 1993), referred to as "Paper III" below, these solutions were used to illustrate a number of problems that occur with voltage clamp of neurones.

Despite providing a useful complement to compartmental modeling techniques, these analytical solutions have a number of weaknesses, in particular:

(i) A uniform distribution of the specific electrical parameters $C_m$ (membrane capacitance per unit area), $R_m$ (resistance of a unit area of membrane) and $R_i$ (cytoplasmic resistivity) is assumed, whereas in reality they may vary from one part of the cell to another,

(ii) Additional *localized* constant conductances away from the soma cannot be incorporated, for example, those due to shunting inhibition (e.g., Rall, 1964; Jack et al., 1975, chapter 7; Koch et al., 1990) or electrode-induced leaks from dendritic recordings, and

(iii) Changing conductances, for example, active or transient synaptic conductances, cannot be included.

This paper will address the first two points, but not the third.

### Reasons for nonuniform passive models

#### Specific membrane resistivity ($R_m$)

Good passive models are an essential foundation for models incorporating active conductances accurately. Under many circumstances the behavior of a neuron may be dominated by active conductances in both soma and dendrites (e.g., Hounsgaard and Midtgaard, 1989). However, in certain situations, for example, at rest when voltage transients are very small, or at very extreme membrane potentials or after pharmacological manipulations, these conductances may reach an effective steady-state, perhaps with a nonuniform distribution.

There is mounting evidence that membrane ion channel densities vary over different parts of many neurones. Both anatomical and electrophysiological data now exist suggesting that different kinds of calcium channel are located preferentially on different classes of dendrite (e.g., Westenbroek et al., 1990, 1992; Hillman et al., 1991). Sodium channels are located predominantly (but nonuniformly) on the somata and apical trunks of pyramidal cells (e.g., Huguenard et al., 1989). Delayed rectifier potassium channels in pyramidal cells may be most dense on the cell body and proximal dendrites (e.g., Trimmer, 1991). Many ion channels open only at thresholds positive to the resting membrane potential (for review, see Llinás, 1988). However, there is now evidence that other conductances, active at rest, may have differential distributions over certain cells, for example the conductance(s) responsible for undershoot after excitatory postsynaptic potentials or EPSPs (Major, 1992, chapter 5; Nicoll et al., 1993). Another potential cause of nonuniform effective $R_m$ would be spatial variations in the distribution of tonically active synaptic conductances (e.g., Holmes and Woody, 1989). No doubt, as further data become available, more examples will be found.

#### Cytoplasmic resistivity ($R_i$)

It is also possible that $R_i$ may be nonuniform. There is evidence that $R_i$ may be of the order of 200–300 Ωcm in many classes of mammalian neuron (e.g., Shelton, 1985; Stratford et al., 1989; Major, 1992; Paper I; Jonas et al., 1993; Thurbon et al., 1994; Major et al., 1994), rather than the more conventional 70 Ωcm (e.g., Barrett and Crill, 1974; Clements and Redman, 1989). Part of this discrepancy may be explained by the observation that a significant fraction of the cross-sectional area of neuronal processes can be occluded by organelles and cytoskeletal elements (e.g., Stevens et al., 1988). In addition, the properties of intracellular water differ from that of pure water or water in electrolyte solutions. For example, self-diffusion coefficients can be two- to sevenfold lower, and microviscosity may be up to 5 times higher in cell water than in pure water (e.g., Clegg, 1984a, b). The effects of organelles, cytoskeleton, and cytomatrix on $R_i$ may well vary over different parts of a neurone.

#### Specific membrane capacitance ($C_m$)

It seems less likely, although not inconceivable, that $C_m$ may vary from one part of a cell to another (see below for modeling electrodes). Different densities of transmembrane proteins or nonuniform lipid composition may affect the dielectric properties of the membrane. Gating currents can occur in the absence of ionic currents and could increase effective $C_m$ locally (although, because this is both a voltage- and frequency-dependent phenomenon (e.g., Takashima, 1976), this kind of nonuniformity violates passive modeling assumptions).

#### *Dendritic shunts*

Additional point shunt conductances may occur both in vitro and in vivo. An example might be where a dendrite has been

impaled by a sharp electrode (e.g., Wong and Stewart, 1992). Localized "shunting" inhibitory conductances may also occur (e.g., Rall, 1964; Jack et al., 1975, chapter 7; Koch and Poggio, 1985).

### *Microelectrodes and micropipettes*

Passive cables need not be neuronal in origin: when a pipette or electrode is introduced onto or into a cell, it behaves very much like an additional process with membrane capacitance (the transmural capacitance) and resistance (the extremely high transmural resistance), and cytoplasmic resistance (the axial resistance of the filling solution and any occlusions). The values of $R_m$, $C_m$ and $R_i$ for the electrode in question will normally be very different from those of the cell!

### *Nonuniformities introduced by simplified representations*

It is common practice to model the effects of dendritic spines by adjusting the values of $C_m$ and $R_m$ in a given dendritic segment to reflect the increase in surface area. If $F_j$ = (area including spines) ÷ (area without spines) for a segment $j$, then $C_m$ is multiplied by $F_j$ and $R_m$ is divided by $F_j$ in that segment (e.g., Shelton, 1985; Rapp et al., 1992). Dendritic shaft diameters, spine densities, or single spine areas generally vary in such a way as to change $F_j$ from one segment to another (e.g., Larkman, 1991), resulting in nonuniform adjusted $R_m$ and $C_m$ (but not $R_i$).

Other simplification procedures may lead to nonuniform parameters, for example, that used by Douglas and Martin (1992): to preserve physical length, surface area, electrotonic length, input impedence, and dendrite-to-soma transfer impedences when dendrites are collapsed together, $R_i$ must be increased. For example, if $N$ identical cylinders of length $l$ and diameter $d$ are combined into one equivalent cylinder of length $l$ and diameter $Nd$, then $R_i$ must be increased by a factor $f^{R_i} = N$ to conserve the electrotonic length $L$ (giving equivalent $L = 2l(f^{R_i}R_i/R_mNd)^{1/2} = 2l(R_i/R_md)^{1/2} =$ original $L$) and to ensure that the total input conductance (infinitely extended cylinders) is the same for both models (so original $Ng_\infty = N(\pi/2)(R_mR_i)^{-1/2}d^{3/2} = (\pi/2) \cdot (R_mR_if^{R_i})^{-1/2}(Nd)^{3/2} = g_\infty$ of equivalent cylinder). Suppose a cell's dendritic segments can be grouped into sets, every member of a given set having the same length and diameter. If the sets contain different numbers of segments, then $R_i$ of the simplified representation will necessarily be nonuniform.

Both of the above electro-morphological simplification procedures can actually be mapped formally onto equivalent procedures that change only the morphology and leave the electrical parameters uniform. Spines can be incorporated into their shafts of origin by the transformation $l^* = lF^{2/3}$, $d^* = dF^{1/3}$ as described in Stratford et al. (1989) and Larkman et al. (1992). Complicated, nonequivalent cylinder dendritic arbors can be simplified into "cartoon" representations (Stratford et al., 1989; Paper I) by performing equivalent cylinder collapses only on groups of dendrites of similar electrotonic lengths and with points of origin close together. Nevertheless, some workers find it advantageous to use procedures that change the electrical parameters nonuniformly.

## Constraining nonuniformities

If the distribution of electrical parameters over a given detailed branching model were completely unconstrained, "core" electrotonic model nonuniqueness might become an intractable problem: many different models might match a given set of experimental waveforms indistinguishably well, but yield substantially different predicted responses for other, untested, input or recording sites (see Discussion in Paper I and below). Some constraints on the possible nonuniformities are necessary if only limited target experimental data are available.

Fortunately, it is unlikely that $C_m$ varies much over a cell, particularly under passive conditions. Accurate independent measurements of $C_m$ could be made from isolated somata, synaptosomes, or from near-spherical cells (e.g., Rosenboom and Lindau, personal communication).

Membrane resistances and shunts influence responses at late times more than at early times (see below). Moreover, the actual *distribution* of $R_m$ may not affect model predictions greatly once one response has been optimized against its experimental counterpart (see Example 2, below). Variations in $R_m$ can be reduced by ion channel blockade. The relative distribution of $R_m$ could be constrained by channel density estimates, for example, using specific binding agents (e.g., Ellisman and Levinson, 1982; Westenbroek et al., 1992) or from cell-attached patch clamping onto as many kinds of process as possible. Electrode-induced shunts can minimized by using tight seal whole-cell recording (e.g., Jonas et al., 1993; Major et al., 1994), and tonic shunting synaptic conductances can be eliminated using neurotransmitter blockers (or channel blockers in some cases).

There might be more of a problem with $R_i$ if it does, indeed, turn out to vary with process diameter or contents. Future studies may help establish some simplifying relationships. Tortuosity and the proportion of cross-sectional area occluded by cytoskeleton and organelles could be estimated using electron microscopy. Ion diffusion rates could be measured with ion-sensitive dyes, such as those used by Jaffe et al. (1992). Dendritic whole-cell recordings (e.g., Stuart et al., 1993) or voltage sensitive dyes (e.g., Fromherz and Vetter, 1992) may prove extremely powerful in combination with morphologically based cable models, and they may help further constrain the possible distribution of electrical parameters in a given cell.

## Methods for dealing with nonuniform models

Compartmental models are sufficiently flexible to incorporate both static and time-varying nonuniformities in the electrical parameters of a model. The compartmental model matrix eigenfunction expansion method (Rall, 1964; Perkel et al., 1981; Holmes et al., 1992) can be used to produce $N$ time constants and amplitudes in nonuniform models with

static parameters, where $N$ is the number of compartments (e.g., Holmes and Woody, 1989). This technique and others, such as implicit numerical integration (Hines, 1984, 1989), can also be very efficient. Arbitrary accuracy can be achieved by increasing the number of compartments (at the cost of slower computations).

Rall (1962) considers the simplified case of transients in a cylinder with two regions of different steady membrane and synaptic conductance densities, but as far as we know there is no published analytical solution for transients incorporating arbitrary branching (with a soma), nonuniformities in $C_m$, $R_m$, and $R_i$, and dendritic shunts. In this paper, the methods used in Papers I and II are extended to obtain separation-of-variables solutions for models with *discontinuous* nonuniformities, i.e., the electrical parameters can be different from one segment to another, but must be constant within a given segment. Smooth spatial variations in electrical parameters can be approximated by using small segments. The analytical solutions have a number of useful features:

(i) the exponential components of response waveforms are given explicitly,
(ii) parameter dependencies are clarified,
(iii) the mapping of infinitely many "raw" electro-morphological[1] models onto a particular, more compact, core electrotonic model is demonstrated (see Discussion), and
(iv) their implementations can be both accurate and efficient.

Systematic comparison of these solutions with the passive modeling methods mentioned above has yet to be undertaken. We note that although the analytical solutions discussed in this and the preceding three papers obtain system time constants from eigenvalues that are the roots of a recursive *transcendental* equation (with sines, cosines, etc.), the matrix eigenfunction method uses the eigenvalues of the compartmental matrix, which can be obtained in a number of ways that are equivalent to finding the roots of its *polynomial* characteristic equation (e.g., Press et al., 1988, chapter 11). Transcendental functions can be approximated by polynomials; as the number of compartments per segment is increased, so the compartmental matrix's characteristic equation should tend to the corresponding cable model's transcendental equation (if both are in terms of the same variable), and the time constants obtained from the two methods should agree exactly. How well they match with typically used compartment sizes has yet to be investigated. As long as the two methods yield similar enough waveforms, any mismatch between their exponential components may be of limited significance for most purposes (see discussion of simplified representations in Paper I).

[1] When referring to models or their parameters, the term "raw" is used in this paper as a concise synonym for "electro-morphological," and "core" is used as a synonym for "electrotonic."

The nonuniform solutions cannot deal with time-varying conductances. If conductance transients have stereotyped waveforms, then discrete time approximations can be made (e.g., Holmes, 1986; Wilson, 1984), with different passive models producing consecutive portions of the transient. The model would be changed after each time step, setting the conductance to its next level. The final voltage distribution of the previous time step would become the initial voltage distribution of the next. However this method is cumbersome, and it cannot deal with additional state variables such as those required for voltage-dependent conductances (e.g., Hodgkin and Huxley, 1952). Active compartmental modeling (e.g., Hines, 1984, 1989; Wilson and Bower, 1989) seems to be a more elegant and appropriate technique for this kind of problem.

The main steps of the derivation mirror those in Papers I and II (Major et al., 1993a, b), whose conventions and symbols are adhered to throughout. See also the List of Symbols and Tables 1 and 2. Where possible, repetition of equations in Papers I and II is avoided. A reference to Eq. I.5, for example, would indicate Paper I, Eq. 5. After the mathematical sections, some applications are given.

## VOLTAGE RECORDING IMPULSE RESPONSE

### Definition of the system

We assume a dendritic morphology composed of uniform cylindrical segments, with every segment labeled by an index $j$. The segments originating from the soma are called the stem segments, and their indices *st* form the set *stems*. Each nonterminal (i.e., parent) segment $p$ gives rise to a number of daughter segments $d$ forming the set $dtrs_p$ (examples in Paper I, Fig. 1). Summations and products are over all the members of the relevant set.

The default or global membrane time constant is $\tau_m = R_m C_m$. Table 2 details the physical and electrical parameters for a segment $j$. Notice the segment-specific "distribution

**TABLE 1 Index conventions**

| | |
|---|---|
| Eigenvalue and eigenfunction index | |
| $n$ | (= 0, 1, 2, . . .), never used as a segment index |
| Segment indices | |
| $j$ | arbitrary |
| $p$ | parent |
| $d$ | daughter |
| $r$ | segment recorded from |
| $e$ | segment stimulated (excited) |
| $c$ | segment in a chain |
| $s$ | soma |
| $st$ | stem segment |
| Set notation | |
| $d \in dtrs_p$ | over all the daughters $d$ of segment $p$ |
| $st \in stems$ | over all the stem segments $st$ |
| $j \in segs$ | over all segments $j$ |
| $c \in chain_j$ | over all segments in direct chain between soma and $j$ (inclusive) |
| $\forall st \in stems$ | for all stem segments $st$ |
| $\mathcal{P}(j)$ | parent of segment $j$ |
| $\mathcal{S}(j)$ | stem segment of sub-tree containing segment $j$ |

**TABLE 2 Parameters for segment *j***

Specific electrical parameter distribution factors

| | |
|---|---|
| $f_j^{C_m}$ | specific membrane capacitance factor [*dimensionless*] |
| $f_j^{R_m}$ | membrane resistivity factor [*dimensionless*] |
| $f_j^{R_i}$ | cytoplasmic resistivity factor [*dimensionless*] |

Raw electro-morphological parameters

| | |
|---|---|
| $l_j$ | physical length [$\mu$m] |
| $d_j$ | diameter [$\mu$m] |
| $C_{m_j}$ | $= f_j^{C_m} C_m$, actual specific membrane capacitance of $j$ [$\mu$Fcm$^{-2}$] |
| $R_{m_j}$ | $= f_j^{R_m} R_m$, actual specific membrane resistivity of $j$ [$\Omega$cm$^2$] |
| $R_{i_j}$ | $= f_j^{R_i} R_i$, actual axial resistivity of $j$ [$\Omega$cm] |
| $g_{shunt_j}$ | shunt conductance at distal end of $j$ (also a core parameter) [nS] |

Core electrotonic parameters

| | |
|---|---|
| $L_j$ | $= l_j/\lambda_j$, electrotonic length of $j$ [*dimensionless*] |
| $\tau_{m_j}$ | $= c_{m_j} r_{m_j} = C_{m_j} R_{m_j} = \epsilon_j \tau_m$, local membrane time constant [ms] |
| $g_{\infty_j}$ | $= (r_{m_j} r_{a_j})^{-1/2} = (\pi/2)(R_{m_j} R_{i_j})^{-1/2} d_j^{3/2}$, input conductance of infinite extension of $j$ [nS] |
| $g_{shunt_j}$ | shunt conductance at distal end of $j$ (also a raw parameter) [nS] |

Other useful combinations of parameters

| | |
|---|---|
| $c_{m_j}$ | $= \pi d_j C_{m_j}$, capacitance per unit length of $j$ [$\mu$Fcm$^{-1}$] |
| $r_{m_j}$ | $= R_{m_j}/\pi d_j$, membrane resistance of a unit length of $j$ [$\Omega$cm] |
| $r_{a_j}$ | $= 4R_{i_j}/\pi d_j^2$, axial resistance per unit length of $j$, [$\Omega$cm$^{-1}$] |
| $\lambda_j$ | $= (r_{m_j}/r_{a_j})^{1/2} = (R_{m_j} d_j/4R_{i_j})^{1/2}$, space constant of segment $j$ [$\mu$m] |
| $\epsilon_j$ | $= \tau_{m_j}/\tau_m = f_j^{C_m} f_j^{R_m}$, local membrane time constant ratio [*dimensionless*] |

factors" multiplying the default-specific electrical parameters. For example, the factor $f_j^{R_m}$ multiplies $R_m$ to give the segment's actual specific membrane resistivity $R_{m_j}$. As a consequence, each segment can have its own local membrane time constant $\tau_{m_j} = \epsilon_j \tau_m$, where $\epsilon_j = f_j^{R_m} f_j^{C_m}$. Without loss of generality we assume that at the soma $f^{C_m} = f^{R_m} = 1$, i.e., that the soma *membrane* is a "reference" against which the rest of the cell's membrane is compared. This allows us to continue to use unsubscripted $\epsilon = \tau_s/\tau_m = g_{sm}/g_s$ as the somatic shunt parameter, where $g_{sm}$ is the lumped soma membrane conductance *before* introduction of any shunt, $g_{shunt}$ (with no subscript $_j$) is the somatic shunt conductance, $g_s = g_{sm} + g_{shunt}$ is the total somatic conductance, $\tau_s = c_s/g_s$ is the effective somatic time constant including the shunt, and $c_s$ is the lumped soma capacitance. A further elaboration of the model is the possibility of an extra shunt conductance to earth, $g_{shunt_j}$, at the distal (furthest from the soma) *end* of each segment $j$: this will complicate the current conservation constraint at the branch point (see below). A shunt at a location within a segment can be achieved by splitting the segment in two and including it at the new branch point.

Time is in dimensional (S.I.) units, but distances are in normalized units of $\lambda_j$, the space constant of segment $j$. The voltage response $V_r(X_r, Z_e, t)$ at electrotonic distance $X_r$ along segment $r$ is desired, after injection at time $t = 0$ of a unit point charge at electrotonic distance $Z_e$ along segment $e$. The system to be solved is defined by the following equations:

For each segment $j$, the cable equation

$$\frac{\partial^2 V_j}{\partial X_j^2} - \tau_{m_j} \frac{\partial V_j}{\partial t} - V_j = 0. \tag{1}$$

The boundary conditions

*At terminations:*

$$g_{\infty_j} \left( \frac{\partial V_j}{\partial X_j} \right)_{X_j = L_j} + g_{shunt_j} (V_j)_{X_j = L_j} = 0, \tag{2}$$

(axial current = current flowing through terminal shunt.)

*At branch points:*

$$g_{\infty_p} \left( \frac{\partial V_p}{\partial X_p} \right)_{X_p = L_p} + g_{shunt_p} (V_p)_{X_p = L_p} = \sum_{d \in dtrs_p} g_{\infty_d} \left( \frac{\partial V_d}{\partial X_d} \right)_{X_d = 0} \tag{3}$$

(axial current conserved.) The somatic boundary condition, voltage continuity constraints, and the initial condition are given by Eqs. I.8–I.11.

## Separation of variables solution

Following Rall (1969) and Paper I, the general solution of the above system of equations, in separable form, is

$$V_r(X_r, Z_e, t) = \sum_{n=0}^{\infty} E_n \psi_{en}(Z_e) \psi_{rn}(X_r) e^{-t/\tau_n} \equiv \sum_{n=0}^{\infty} A_{n_{er}} e^{-t/\tau_n}, \tag{4}$$

where

$$\psi_{jn}(X_j) = \kappa_{jn} [\cos \alpha_{jn}(L_j - X_j) + \mu_{jn} \sin \alpha_{jn}(L_j - X_j)] \tag{5}$$

are the spatial eigenfunctions, and

$$\tau_n = \tau_m/(1 + \alpha_n^2) = \tau_{m_j}/(1 + \alpha_{jn}^2) \tag{6}$$

are the time constants, i.e.,

$$\alpha_{jn} = (\tau_{m_j}/\tau_n - 1)^{1/2}. \tag{7}$$

The $\alpha_{jn}$ are the eigenvalues for the $j$th segment and may be termed the local or segment eigenvalues, whereas the $\alpha_n$ may be termed the global or cell eigenvalues. If $\tau_{m_j} < \tau_n$, then $\alpha_{jn}$ is an imaginary number. (Imaginary $\alpha_n$ values can be avoided by ensuring that the global default (=soma membrane) $\tau_m$ is greater than or equal to all of the local dendritic $\tau_{m_j}$ values. Because the soma is lumped, we are free to choose how much of its total conductance is assigned to its membrane, and how much to its shunt.)

The factors $\kappa_{jn}$, which ensure voltage continuity at branch points, satisfy the iterative definition

$$\kappa_{jn} = \prod_{c \in chain_j} (\cos \alpha_{cn} L_c + \mu_{cn} \sin \alpha_{cn} L_c)^{-1}, \tag{8}$$

where the elements of $chain_j$ are the indices of every segment $c$ in a "chain of direct descent" ("mainline"), starting with the stem segment of the tree containing $j$, and ending with segment $j$ itself.

The $\mu_{jn}$, obtained using current conservation and voltage continuity at branch points, are defined recursively as

$$\mu_{pn} = \frac{1}{\alpha_{pn} g_{\infty_p}} \cdot \left\{ g_{\text{shunt}_p} - \sum_{d \in dtrs_p} \alpha_{dn} g_{\infty_d} \left( \frac{1 - \mu_{dn} \cot \alpha_{dn} L_d}{\cot \alpha_{dn} L_d + \mu_{dn}} \right) \right\}, \quad (9)$$

for parent $p$ and daughter $d$ branches, with the condition for terminal segments

$$\mu_{jn} = \frac{g_{\text{shunt}_j}}{\alpha_{jn} g_{\infty_j}}. \quad (10)$$

The global eigenvalues $\alpha = \alpha_n$, $n = 0, 1, \ldots$ are given by the roots of the recursive transcendental equation,

$$g_s[1 - \epsilon(1 + \alpha^2)] \equiv g_{\text{shunt}} - \alpha^2 g_{\text{sm}} = \sum_{st \in stems} \alpha_{st} g_{\infty_{st}} \left( \frac{1 - \mu_{st} \cot \alpha_{st} L_{st}}{\cot \alpha_{st} L_{st} + \mu_{st}} \right), \quad (11)$$

where

$$\alpha_j^2 = \epsilon_j (1 + \alpha^2) - 1, \quad (12)$$

and the $\mu_j$ are defined by Eqs. 9 and 10, dropping the subscript $n$. The root-finding algorithm described in the Implementation section below can deal with imaginary global or local $\alpha$ values.

The position-independent ("Electrical") component $E_n$ of the amplitude term $A_{n_{er}}$ may be determined using techniques from complex analysis (e.g., Priestley, 1985; see Appendix 1 below for details) and can be written as

$$E_n = \left[ g_{\text{sm}} \tau_{\text{m}} + \frac{1}{2} \sum_{j \in segs} v_{jn} \right]^{-1}, \quad (13)$$

where $v_{jn}$ is defined by

$$v_{jn} \equiv \tau_{\text{m}_j} g_{\infty_j} \kappa_j^2 \{ L_j (1 + \mu_{jn}^2) + [(1 - \mu_{jn}^2) \sin 2\alpha_{jn} L_j + 4\mu_{jn} \sin^2 \alpha_{jn} L_j] / 2\alpha_{jn} \}, \quad (14)$$

except where $\alpha_0 = 0$, in which case Eq. I.36 applies. We note that $g_s \tau_s = g_{\text{sm}} \tau_{\text{m}} = c_s$, and $\tau_{\text{m}_j} g_{\infty_j} = c_{\text{m}_j} \lambda_j$, where $c_{\text{m}_j}$ is the capacitance per unit length of segment $j$, so $E_n$ has units of 1/capacitance. As with the uniform case (Paper I), an alternative derivation of the amplitude terms is possible using a modified orthogonality relation (Churchill, 1942).

## PERFECT VOLTAGE CLAMP IMPULSE RESPONSES

The solutions are similar to those given in Paper II. The definition of $\kappa_{jn}$ is given by Eq. I.28 with $\alpha_n$ being replaced by $\alpha_{dn}$, and $\kappa_{st} = 1$. The eigenvalues are the roots of the recursive transcendental equation (Eq. II.6), replacing $\alpha$ with $\alpha_{st}$, using the definition of $\mu_{jn}$ above (Eqs. 9 and 10). $E_{n_{st}}$ is given by

$$E_{n_{st}} = \begin{cases} \left[ \frac{1}{2} \sum_{j \in subtree(st)} v_{jn} \right]^{-1} & \text{if } \left\{ \begin{array}{c} \cot \alpha_{st,n} L_{st} + \mu_{st,n} = 0 \\ \text{and} \\ \mathcal{S}(e) = \mathcal{S}(r) = st \end{array} \right\} \\ 0 & \text{otherwise} \end{cases} \quad (15)$$

where $\mathcal{S}(j)$ is the *stem* segment of $j$ (derivation in Appendix 2). We note that the summation is only over segments in the subtree with stem $st$, from which the global eigenvalue $\alpha_n$ was generated. The clamp point is taken to belong to all subtrees. The responses to a dendritic charge impulse (case I), with the soma clamped to zero, are given by Eqs. II.15–II.17, and II.19 with $\alpha_n$ replaced by $\alpha_{\mathcal{S}(e)n}$. Likewise, the responses to a somatic voltage impulse command (case II) are given by Eqs. II.21–II.24, replacing $\alpha_n$ by $\alpha_{\mathcal{S}(r)n}$.

### Nonsomatic voltage clamp

As discussed in Paper II, rather than derive new (and more complicated) solutions for dendritic voltage clamp points, it is easier to re-label a model, assigning a new "soma" at the clamp point and replacing the original soma with a short cylinder of the correct surface area.

## OTHER RESULTS

### Imperfect voltage clamp impulse responses

The discussion of imperfect voltage clamp in Paper II also applies, with trivial modifications, to nonuniform cables with extra dendritic shunts. The series conductance $g_{\text{ser}}$ is again added to the somatic $g_{\text{shunt}}$ for the transcendental equation (Eq. 11). The expression for $E_n$ given above (Eq. 13) is used. The responses to synaptic inputs (case I) are given by Eqs. II.39 and II.40. Eqs. II.41 and II.42 can be used to obtain the responses to voltage command impulses (case II).

### Responses to arbitrary inputs

The *linearity* of the system can be exploited to obtain the response to any arbitrary current input, voltage command, or initial voltage distribution, by convolution (e.g., Jack et al., 1975, chapter 13). Details for obtaining the responses to current or voltage command steps, short pulses, alpha functions, and multi-exponential functions are given in Papers I and II. Where appropriate, apply Eqs. I.46–I.52, II.26–II.29, II.31, and II.43–II.47. Use the denominator of $\tilde{A}_s$ in Eq. 23 (Appendix 1, below) instead of II.35. The nonuniform Laplace transform solution $\tilde{G}$, and the definition of $\tilde{\mu}_j$ (Eq. 20) given in Appendix 1, below, should be used when required, setting $p = 0$ for steady-state terms, and $p = -$(input rate constant) for lumped terms of smoothly changing inputs. As before, *conductance* inputs are not considered here: compartmental models should be used in such cases.

## Parameter dependence

If the distribution factors $f^{R_m}$, $f^{C_m}$ and $f^{R_i}$ are fixed, then the discussion of parameter dependence in Papers I and II still holds. These factors can be thought of as being "quasi-morphological" in their effect. The time constants will be proportional to, and the $E_n$ will be inversely proportional to, global $C_m$. It can be shown from Eqs. 9, 10, and I.39–I.41 that the $\alpha_n$ are proportional to global $R_m^{1/2}$, and inspection of Eq. 13 shows that the $E_n$ will be independent of $R_m$, as in the uniform case. If the various shunts are either very small or very large (e.g., voltage clamp) compared with the $\alpha_{jn}$, then the $\alpha_n$ are proportional to $R_i^{-1/2}$, and the $E_n$ are independent of $R_i$. As in the uniform case, shunts and $R_m$ have their effects predominantly at late times of responses, $C_m$ is the only global parameter effecting fast amplitudes of impulse responses, and fast time constants are proportional to $R_iC_m$. The dependencies on the distribution factors are not considered in detail here, although they are illustrated in some of the examples below. In essence, changes in $f^{R_m}$ will only affect late times, changes in $f^{R_i}$ will affect early times, and late times if there are nonuniformities in the local membrane time constant (taking shunts into account), and changes in $f^{C_m}$ should affect responses at all times. The extent of these influences will be very dependent on the locations of the stimulation and recording sites relative to the zones changed.

## Implementation

ANSI-C programs have been written for both voltage recording and voltage clamp. Using Eqs. 6 and 7, dropping subscripts $n$, the transcendental equation (Eq. 11) can be expressed in terms of possible time constants $\tau$. Its roots are the required system time constants $\tau_n$, which can be found with recursive root-finding algorithms like those described in Papers I and II. Brent's method of bracketing, then inverse quadratic interpolation or bisection, repeated as appropriate (Press et al., 1988, pp. 267–269), typically yields a three- to fourfold increase in speed over repeated bisection alone. Singularity clashes and "lost roots" are again avoided by minor adjustments to the lengths of the segments involved. For imaginary $\alpha_j = i\beta_j$, expressions are used based on the identities $\cosh \beta_j = \cos i\beta_j$ and $i \sinh \beta_j = \sin i\beta_j$.

In addition, a direct fitting program has been written that uses a simplex algorithm (Nelder and Mead, 1965; Press et al., 1988, pp. 305–309) to match a model's response to a target waveform. Some parts of the model can be varied while others are held constant. This is useful in hybrid electrode-cell models (see Example 3, below), where the electrode parameters are known, but those of the cell need to be optimized against an experimental response. To keep the number of free parameters from growing too large, a fixed distribution of $f^{R_m}$, $f^{C_m}$ and $f^{R_i}$ must be specified over the variable part of the model. The programs have been tested extensively against equivalent nonuniform compartmental model output, and in general run several times faster than a package using explicit

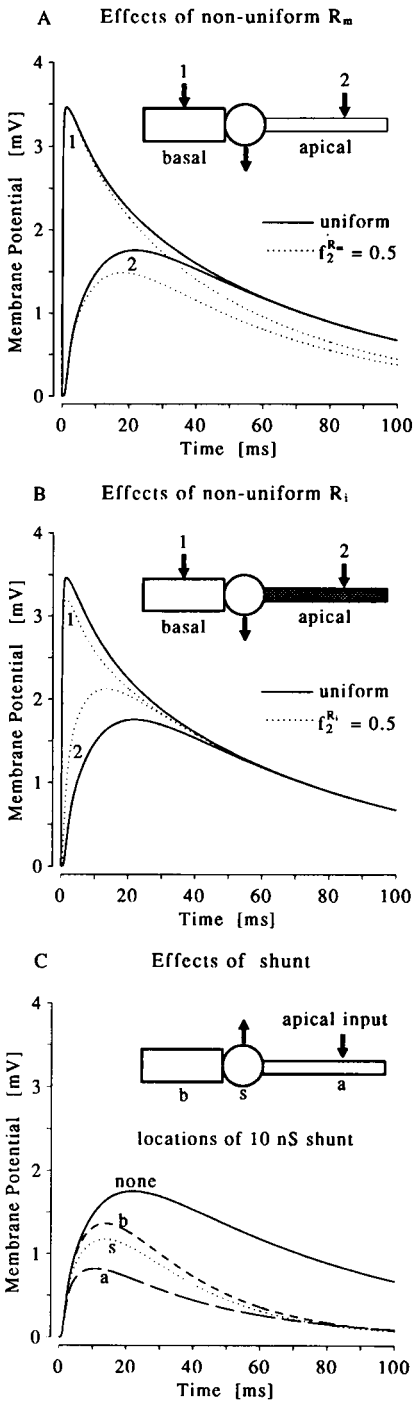


FIGURE 1 Two cylinder + soma simplified representation of a layer III visual cortical pyramidal neuron (Example 2 in Paper I). Soma diameter $d_s$ 15 μm, basal length 1000 μm, diameter 10 μm, apical length 1500 μm, diameter 4 μm; 1 pC point charges injected into one of arrowed sites labeled 1 (basal, 500 μm from soma) or 2 (apical, 1000 μm from soma). All voltage responses recorded from soma. Waveform components listed in Table 3. Solid lines are responses of default model with uniform global electrical parameters: $C_m$, 0.7 μFcm$^{-2}$; $R_m$, 100,000 Ωcm$^2$; $R_i$, 250 Ωcm; no shunt. Other responses are from models with *one* of these parameters nonuniform. (*A*) Apical $R_m$ halved ($f_2^{R_m}$ = 0.5, dotted lines). (*B*) Apical $R_i$ halved ($f_2^{R_i}$ = 0.5, dotted lines). (*C*) A 10-nS shunt at one of three locations: soma (s, *dotted line*), basal (b, 500 μm from soma, *dashed line*), or apical (a, 1000 μm from soma, *long dashed line*): effect on the responses to the apical input. The response of the default model with no shunt is the solid line.

forward Euler integration (Clements, 1986). Further benchmarking and optimization is required.

## APPLICATIONS

All the waveforms illustrated below were generated by the programs just described, and they have been checked against equivalent nonuniform compartmental model output.

### Example 1. Two cylinder + soma models

A simplified representation of a layer III visual cortical pyramidal neurone from an adult rat is shown in Fig. 1, with details of model parameters in the legend. A *camera lucida* drawing and dendrogram of the original cell, together with a description of how the representation was obtained, is given in Paper I. The nonuniform analytical solution is illustrated by comparing models incorporating one nonuniform feature at a time against a default uniform model with biologically plausible parameters.

In Fig. 1 *A*, the nonuniform model has its apical $R_m$ halved with respect to the default. The final decay of the reduced apical $R_m$ model is faster than that of the default model. Because in the nonuniform model the apical membrane discharges more rapidly than the basal, the responses to apical and basal inputs no longer converge at late times, and charge no longer equalizes throughout the cell. The response to the apical input is changed earlier and more markedly than that to the basal input. At early times the responses are not altered from those of the default model. This impression is confirmed by inspecting the values of the waveform components, the first 10 of which are listed in Table 3. Compared with the default uniform model, the reduced apical $R_m$ model has a faster $\tau_0$ and unequal $A_0$ values for the two different input sites, the apical one being smaller than the basal. However, the faster time constants of the two models agree to within two decimal places, for $n > 2$, as do the corresponding amplitude terms for $n > 8$ for the basal and $n > 10$ for the apical (not shown). This example confirms that the $R_m$ distribution affects only relatively late parts of responses, changing both the slow time constants and their associated amplitudes.

By contrast, changes in the $R_i$ distribution affect *early* parts of responses (but not late parts in the case of uniform $\tau_m$ and no shunts). Fig. 1 *B* illustrates what happens when the apical $R_i$ is halved from its default value. The slowest time constants $\tau_0$ and amplitudes $A_0$ of the two models are now the same, and all the responses converge at late times, as charge equalizes. However, the nonuniform model's responses at early times differ from the default model's. The changes are most pronounced and last longest in the case of the apical input. Time constants other than $\tau_0$ are faster in the reduced apical $R_i$ model than in the default, and the pattern of amplitudes is much altered. The difference between the apical and basal responses is smaller in the reduced apical $R_i$ model, reflecting the reduced axial resistance between the two input sites.

Fig. 1 *C* shows the effect of a 10-nS shunt upon the apical response, and how this changes with the location of the shunt. The waveform components of the shunt models are listed in the lower half of Table 3. Of the three locations, the shunt at the input site causes the earliest changes and reduces the peak somatic voltage the most. The shunt furthest from the input site, i.e., the basal one, has the smallest effect of the three. However, the shunt at the soma reduces $\tau_0$ the most, because it has the greatest "access" to the whole cell, whereas the apical shunt reduces $\tau_0$ the least, having the worst access. Note that, irrespective of location, shunts only affect responses at late times: the early parts of the responses superimpose. The time constants with $n > 5$ agree with those

**TABLE 3 Two cylinder + soma models***

| $n$ | 0 | 1 | 2 | 3 | 4 | 5 | 6 | 7 | 8 | 9 |
|---|---|---|---|---|---|---|---|---|---|---|
| Default uniform model | | | | | | | | | | |
| $\tau_n$ | 70.00 | 10.14 | 1.80 | 0.82 | 0.56 | 0.32 | 0.21 | 0.17 | 0.13 | 0.10 |
| $A_{n_{1s}}$ | 2.80 | 1.01 | −0.21 | −0.56 | 0.47 | 0.04 | −2.57 | −4.55 | −0.40 | 0.45 |
| $A_{n_{2s}}$ | 2.80 | −2.58 | −0.05 | −3.73 | 4.65 | −0.21 | −0.79 | −1.72 | 1.56 | 2.51 |
| Apical $f^{R_m} = 0.5$ | | | | | | | | | | |
| $\tau_n$ | 52.19 | 9.15 | 1.76 | 0.82 | 0.56 | 0.32 | 0.21 | 0.17 | 0.13 | 0.10 |
| $A_{n_{1s}}$ | 3.02 | 0.79 | −0.22 | −0.55 | 0.47 | 0.04 | −2.61 | −4.51 | −0.39 | 0.45 |
| $A_{n_{2s}}$ | 2.56 | −2.32 | −0.05 | −3.70 | 4.60 | −0.18 | −0.81 | −1.70 | 1.54 | 2.53 |
| Apical $f^{R_i} = 0.5$ | | | | | | | | | | |
| $\tau$ | 70.00 | 5.78 | 1.09 | 0.62 | 0.32 | 0.20 | 0.15 | 0.10 | 0.08 | 0.06 |
| $A_{n_{1s}}$ | 2.80 | 0.81 | −0.82 | 0.47 | 0.03 | −4.83 | −2.21 | 0.51 | 0.42 | −0.42 |
| $A_{n_{2s}}$ | 2.80 | −1.96 | −0.74 | −1.68 | 0.09 | 5.32 | −3.58 | −0.14 | −2.52 | 2.20 |
| Basal $g_{shunt} = 10$ nS | | | | | | | | | | |
| $\tau_n$ | 27.17 | 8.64 | 1.79 | 0.82 | 0.56 | 0.32 | 0.21 | 0.17 | 0.13 | 0.10 |
| $A_{n_{2s}}$ | 3.32 | −3.14 | −0.03 | −3.71 | 4.68 | −0.29 | −0.70 | −1.82 | 1.65 | 2.47 |
| Soma $g_{shunt} = 10$ nS | | | | | | | | | | |
| $\tau_n$ | 26.74 | 9.22 | 1.80 | 0.79 | 0.55 | 0.32 | 0.21 | 0.17 | 0.13 | 0.10 |
| $A_{n_{2s}}$ | 3.01 | −2.76 | −0.04 | −3.90 | 4.79 | −0.21 | −0.73 | −1.81 | 1.58 | 2.46 |
| Apical $g_{shunt} = 10$ nS | | | | | | | | | | |
| $\tau_n$ | 38.16 | 5.50 | 1.80 | 0.80 | 0.54 | 0.31 | 0.21 | 0.17 | 0.13 | 0.10 |
| $A_{n_{2s}}$ | 1.27 | −0.98 | −0.05 | −3.25 | 3.94 | 0.03 | −0.80 | −1.66 | 1.38 | 2.72 |

* Units: $\tau_n$, ms; $A_{n_{er}}$, mV.

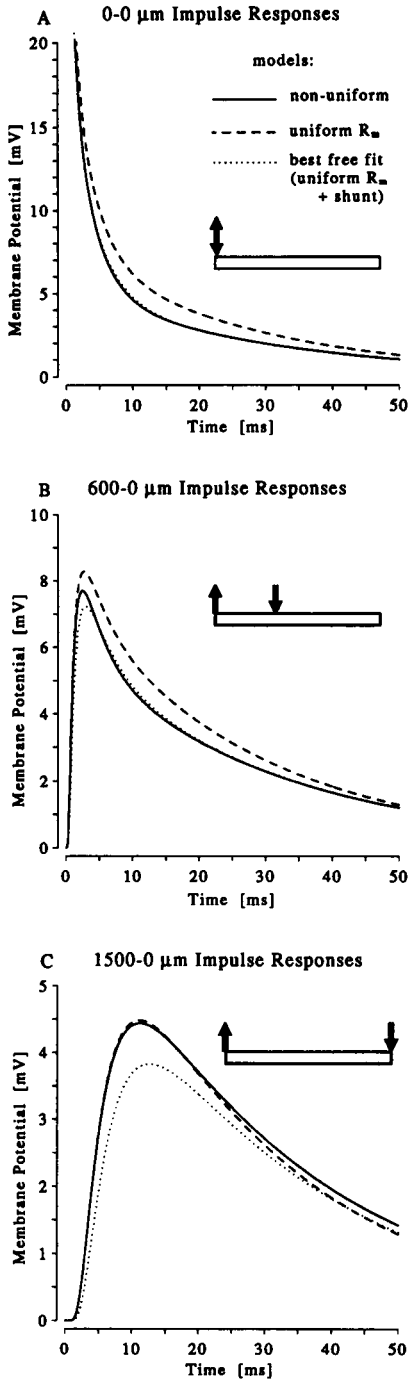


FIGURE 2 Single cylinder models: nonuniform $R_m$ vs. uniform $R_m$ with and without a shunt. Length 1500 μm, diameter 4 μm. The responses to a 1 pC point charge of three of the models in Table 4 are compared (waveform components in Table 5). Recording site for all waveforms is the left hand end of the cylinder (0 μm). Note the different voltage scales in the three panels. Solid lines: "true" model, cylinder divided into five equal segments, $f^{R_m}$ doubles from one segment to next moving from left to right. Dashed lines: membrane conductance of true model spread evenly over whole cylinder to give a uniform $R_m$. Dotted lines: uniform $R_m$, and shunt at left hand end of cylinder; parameters $R_m$, $C_m$, $R_i$, and $g_{shunt}$ from optimum unconstrained fit to response of nonuniform $R_m$ model with input site at left hand end (0 μm). This model illustrates the relatively minor errors that arise for this geometry and centrifugally increasing $R_m$, when uniform $R_m$ is incorrectly assumed but the fitter allows a somatic shunt. More quantitative comparisons of the models' responses are given in Table 4. (*A*) Stimulation site left hand end (0 μm). The best free fit model response agrees extremely closely with the target true nonuniform model response, but the evenly-spread membrane conductance model ("uniform $R_m$") gives a very different waveform. (*B*) Stimulation site 600 μm along cylinder. The nonuniform and best fit models still agree well. (*C*) Stimulation site right hand end of cylinder (1500 μm from left). The evenly-spread conductance model now gives the best match to the nonuniform model.

of the default (no shunt) model to within two decimal places irrespective of shunt location. The amplitudes of the faster components tend to those of the no-shunt model.

In summary, the distribution of $R_m$ and shunts only affects late parts of responses, whereas the distribution of $R_i$ affects early parts (and can affect later parts when some parts of the cell discharge more rapidly than others; not shown). Changes in $C_m$ distribution affect all parts of waveforms (not illustrated).

## Example 2. Fits to single cylinder model with nonuniform $R_m$

An important part of passive neural modeling is parameter estimation from experimental data. Given a measured cell morphology and a short pulse response recorded from the same cell, what is the range of electrical parameters that is compatible with the data? An important assumption commonly made in the absence of any quantitative information about the distribution of passive membrane conductances is that dendritic $R_m$ is uniformly distributed, allowing perhaps for the possibility of increased somatic conductances or a somatic shunt. Suppose in reality the distribution of dendritic $R_m$ is highly nonuniform; what kind of errors may result from falsely assuming that it is uniform? Fleshman et al. (1988) and Clements and Redman (1989) compared short pulse responses recorded from spinal motoneurones using sharp electrodes to the equivalent responses of various kinds of morphologically based compartmental model, after parameter optimization. Models with either a step increase in $R_m$ from soma to dendrites (equivalent to a somatic shunt), or with $R_m$ increasing monotonically from soma to dendritic tips, allowed good fits to the experimental data. However, uniform $R_m$ models without a shunt frequently proved to be incompatible with the real neurones' responses.

Another (minimalist) illustration of this issue is presented in Fig. 2 and Tables 4 and 5, using a single cylinder representation. The "true" model cell consists of five 300 μm long, diameter 4 μm segments in a chain, with $f^{R_m}$ doubling from one segment to the next, starting from unity on the left. Global $C_m = 0.7$ μFcm$^{-2}$, $R_m = 15{,}600$ Ωcm$^2$, $R_i = 250$ Ωcm, and there are no shunts. The overall 16-fold variation in $R_{m_j}$ is hopefully far more extreme than would be encountered in typical cells in quiescent preparations such as brain slices. Increases in $R_m$ away from the soma could be due to a number of factors. More ion channels may occur naturally in the somatic membrane, with a gradual fall-off with distance away from the soma. Alternatively, if a cell has been impaled by a microelectrode containing high concentrations of ions

**TABLE 4 Summary of single cylinder models**

| Model | $C_m$ | $R_m$ | $R_i$ | $g_{shunt}$ | C.V.$_0$* | C.V.$_{600}$* | C.V.$_{1500}$* | mean C.V.† |
|---|---|---|---|---|---|---|---|---|
| | $\mu$Fcm$^{-2}$ | $\Omega$cm$^2$ | $\Omega$cm | nS | | | | |
| Uniform $R_m$ | 0.7 | 40,300 | 250 | 0.00 | 0.313 | 0.20 | 0.06 | 0.17 |
| Best free fit | 0.728 | 61,500 | 289 | 1.60 | 0.036 | 0.08 | 0.17 | 0.11 |
| Fixed $C_m$ fit | 0.7 | 62,400 | 280 | 1.63 | 0.037 | 0.06 | 0.12 | 0.07 |
| fixed $R_i$, $C_m$ fit | 0.7 | 47,200 | 250 | 1.09 | 0.081 | 0.08 | 0.17 | 0.11 |

* Fit coefficient of variation between given model response and that of nonuniform $R_m$ model (i.e., fit SD/mean value of target waveform over fit interval of 0.1–100 ms); subscripted numbers are stimulation locations, in $\mu$m from left hand end of cylinder. Recording always from left hand end of cylinder.
† Mean c.v. over six stimulus locations (0, 300, 600, 900, 1200 and 1500 $\mu$m from left hand end).

**TABLE 5 Waveform components from single cylinder models in Table 4***

| $n$ | 0 | 1 | 2 | 3 | 4 | 5 | 6 | 7 | 8 | 9 |
|---|---|---|---|---|---|---|---|---|---|---|
| Nonuniform $R_m$ model | | | | | | | | | | |
| $\tau_n$ | 30.96 | 3.38 | 0.96 | 0.44 | 0.25 | 0.16 | 0.11 | 0.08 | 0.06 | 0.05 |
| $A_{n_{0,0}}$ | 5.23 | 16.17 | 15.77 | 15.44 | 15.28 | 15.16 | 15.21 | 15.21 | 15.20 | 15.18 |
| $A_{n_{600,0}}$ | 6.03 | 6.44 | −12.05 | −12.60 | 4.43 | 15.16 | 4.90 | −12.17 | −12.37 | 4.56 |
| $A_{n_{1500,0}}$ | 7.15 | −14.83 | 15.31 | −15.24 | 15.19 | −15.16 | 15.16 | −15.17 | 15.17 | −15.16 |
| Uniform $R_m$ model | | | | | | | | | | |
| $\tau_n$ | 28.23 | 3.50 | 0.96 | 0.44 | 0.25 | 0.16 | 0.11 | 0.08 | 0.06 | 0.05 |
| $A_{n_{0,0}}$ | 7.58 | 15.16 | 15.16 | 15.16 | 15.16 | 15.16 | 15.16 | 15.16 | 15.16 | 15.16 |
| $A_{n_{600,0}}$ | 7.58 | 4.68 | −12.26 | −12.26 | 4.68 | 15.16 | 4.68 | −12.26 | −12.26 | 4.68 |
| $A_{n_{1500,0}}$ | 7.58 | −15.16 | 15.16 | −15.16 | 15.16 | −15.16 | 15.16 | −15.16 | 15.16 | −15.16 |
| Best free fit model | | | | | | | | | | |
| $\tau_n$ | 31.10 | 3.95 | 1.14 | 0.52 | 0.30 | 0.19 | 0.13 | 0.10 | 0.08 | 0.06 |
| $A_{n_{0,0}}$ | 5.11 | 13.51 | 14.27 | 14.44 | 14.50 | 14.52 | 14.54 | 14.55 | 14.56 | 14.56 |
| $A_{n_{600,0}}$ | 6.04 | 5.51 | −11.14 | −11.99 | 4.12 | 14.53 | 4.74 | −11.64 | −11.89 | 4.34 |
| $A_{n_{1500,0}}$ | 6.59 | −13.70 | 14.33 | −14.46 | 14.51 | −14.53 | 14.55 | −14.55 | 14.56 | −14.56 |

* Units: $\tau_n$, ms; $A_{n_{cr}}$, mV. 1 pC impulses.

in solution, there may be ionic gradients from soma to dendrites, resulting in greater availability of charge carriers to cross membrane channels nearer the soma than further away.

Four different models are compared to the true one (details in Table 4):

(i) A model where the specific membrane conductance $G_m = 1/R_m$ is the average of the $G_m$ values of all the segments, i.e., the *total* membrane conductance is the same as in the true model, but it is evenly distributed ("smeared");
(ii) A model obtained using the standard fitting protocol of this laboratory: $C_m$, $R_m$, $R_i$, and a "somatic" $g_{shunt}$ (at left-hand end) are free parameters of a simplex optimization routine that minimizes the sum of the errors squared between model response and target "true cell" response, given the same stimulus. In this case 1 pC impulses into the left hand end of the cylinder were compared, recording from the same location. A uniform $R_m$ is assumed throughout the cylinder. The optimum free fit model is given in Table 4. Reassuringly, $C_m$ and $R_i$ are very close to their correct values;
(iii) As in (ii), but with $C_m$ constrained to the correct value of 0.7 $\mu$Fcm$^{-2}$;
(iv) As in (ii), but with both $C_m$ and $R_i$ constrained to their correct values.

The predictions of the four models can be compared to the output of the true model in a number of different ways. Impulses of 1 pC were injected into a number of different input sites, with recording from the left hand end ("soma"). A visual impression comparing (i) and (ii) to the true model is illustrated in Fig. 2. Surprisingly, the optimum free fit model leads to predictions of responses from other stimulus sites that are not seriously in error. The smeared $G_m$ model, however, gives very inaccurate impulse responses from stimulation of proximal (left hand) sites.

More objective scoring of the different models is possible. One measure of goodness of fit that is independent of the stimulus size (and only weakly dependent on model dimensions and fit interval) is the fit C.V. or coefficient of variation. This is equal to the root mean squared deviation (fit S.D.) between the two waveforms divided by the mean value of the target waveform over the same interval. This is a more helpful measure, in some ways, than the fit S.D., which suffers from being proportional to the stimulus magnitude and approximately inversely proportional to model capacitance. Fit C.V.s allow useful comparisons to be made between noise-free fits across a wide range of different modeling situations. The average fit C.V. of responses from six test input sites is computed for each model with respect to the true model (see Table 4). Overall, the fixed $C_m$ fit gives the best predictions, followed closely by the other two fit models. The worst model is the one with uniformly smeared $G_m$, except its responses to distal (right hand) inputs are closer than its rivals' to those of the true model.

The first 10 waveform components of the waveforms in Fig. 2 are listed in Table 5. It can be seen that the optimum

free fit model has similar time constants to the true (nonuniform $R_m$) model. The faster time constants ($n > 1$) of the uniform $R_m$ (averaged $G_m$) model are indistinguishable from those of the true model to within two decimal places. However, its slowest time constant is about 10% faster than $\tau_0$ of the true model, and its slowest amplitude does not change with stimulation site, so it is unable to follow the 40% variation in $A_0$ of the true model. The best fit model's amplitudes are all fairly close approximations to those of the true model, whatever the stimulation site.

These simulations need to be extended to more realistic branching geometries, and to actual measured distributions of relative ion channel density (and perhaps $R_i$), as these become available. As a preliminary exercise, however, they are encouraging: even a large "centrifugal" increase in $R_m$ can be compensated for by a point shunt at the "soma," with only comparatively minor errors resulting in the model predictions.

## Example 3. Nonsumming interactions between an electrode and the two cylinder + soma model

A particularly relevant question for electrophysiologists is, "if an electrode produces a given extracellular control artefact in response to a test stimulus, and is then used to stimulate and record from a cell, what is the electrode's *actual* distorting effect on the cell's response to the same stimulus?" To simplify matters, assume that the electrode resistance does not change with impalement/whole-cell recording. (This is unrealistic, particularly in the latter case.) Assume also that the artefact is entirely capacitative, i.e., there are no polarization effects or dielectric breakdown (see Purves, 1981; Major, 1992, chapter 3), and that capacitance neutralization, if available, has already been performed as well as possible. Purves (1981, p. 49) has reported that for a nondistributed electrode capacitance, even with optimal capacitance compensation, the electrode-amplifier circuit 10–90% rise time $t_{1090_{comp}} \approx 2(t_{1090_{el}} t_{1090_{amp}})^{1/2}$, where $t_{1090_{el}}$ is the uncompensated 10–90% rise time of the electrode, and $t_{1090_{amp}}$ is that of the amplifier. What remains after capacitance compensation is effectively an uncompensatable capacitative artefact. A physiologist might instinctively subtract the extracellular control from the response recorded from the cell, to obtain a "cell alone" response. This maneuver unfortunately is misguided, because it is based on a mathematical fallacy, that the responses of the cell and the electrode simply sum. When the electrode is "added" to the cell, a *new system* is created, and "the whole is greater than the sum of its parts!" The electrode now has to discharge to earth *via* the cell, rather than directly via its tip, and the cell has an extra (perhaps distributed) capacitance attached to its soma. Nonsumming interactions are touched on in Paper II, Fig. 3.

A simulation of this nonsumming cell-electrode interaction is shown in Fig. 3. The cell model has the same parameters as the apical $f^{R_m} = 0.5$ model in Example 1A (see Fig. 1 legend), except there is a 10 nS somatic shunt (about what one might expect for a typical intracellular impalement

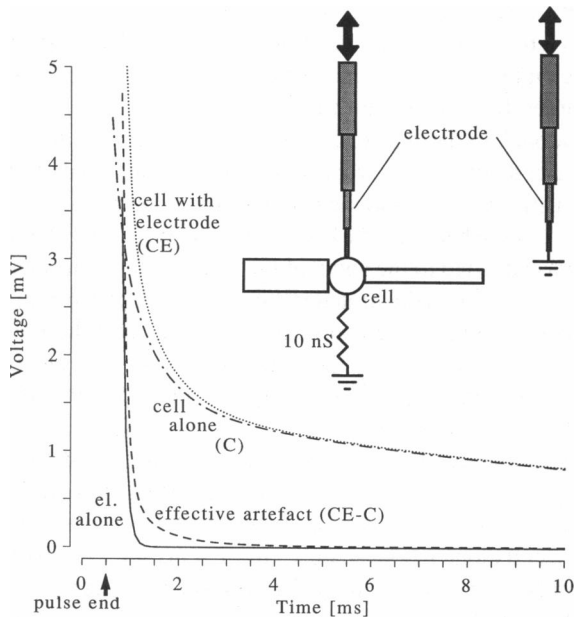


FIGURE 3 Nonsumming cell-electrode interaction. Cell as in Example 1A, with 10-nS shunt at soma. Details of electrode in Table 6. A short square current pulse (1 nA × 0.5 ms) is injected into the wide end of an electrode with its tip earthed. The electrode artefact, i.e., the voltage at the wide end, is recorded (*solid line* marked "el. alone"). The same current pulse is injected directly into the soma of the nonuniform $R_m$ two-cylinder + soma model, and the voltage response at the soma is measured (*dot-dashed line* marked "cell alone (C)"). The tip of the electrode is then attached to the cell, at the soma, so that their interiors become continuous. The current pulse is again injected into the wide end of the electrode. The voltage recorded at the wide end of the electrode is the dotted line marked "cell with electrode (CE)". Finally, the response of the cell alone is subtracted from that of the cell-electrode system to obtain the "effective artefact CE-C" (*dashed line*). The waveform components of the various responses are listed in Table 7.

of this kind of cell: see Major, 1992, chapter 4). The electrode has the same global parameters as the cell; other details are given in Table 6. It is within the range used for intracellular recordings, with a resistance of 113 MΩ, and a stray capacitance to earth of 1 pF. Current pulses of magnitude +1 nA and duration 0.5 ms were used in all cases.

Current was injected into the wide end of the electrode, with its tip earthed (equivalent to being in the extracellular

**TABLE 6 Details of electrode model**

| | | |
|---|---|---|
| Electrode | $f^{R_i}$ | 0.04 |
| seg. 4 (wide end) | $l$ | 400 μm |
| | $d$ | 4.0 μm |
| | $f^{R_m}$ | 8000 |
| | $f^{C_m}$ | 0.0114 |
| seg. 3 | $l$ | 250 μm |
| | $d$ | 2.0 μm |
| | $f^{R_m}$ | 4000 |
| | $f^{C_m}$ | 0.0227 |
| seg. 2 | $l$ | 200 μm |
| | $d$ | 1.0 μm |
| | $f^{R_m}$ | 2000 |
| | $f^{C_m}$ | 0.0455 |
| seg. 1 (tip) | $l$ | 150 μm |
| | $d$ | 0.5 μm |
| | $f^{R_m}$ | 1000 |
| | $f^{C_m}$ | 0.0909 |

solution, see Fig. 3 *inset*, right). The nonuniform perfect voltage clamp solution was used in this case, with the electrode tip clamped to zero. The extracellular artefact, or voltage recorded from the wide end of the electrode, is the solid line "el. alone" in the figure. Current was injected into the soma of the cell with no electrode attached (not illustrated), but the shunt still in place, and the response recorded from the soma is the dot-dashed line marked "cell alone (C)". The electrode tip was attached to the soma of the cell, so that their interiors were continuous (illustrated in Fig. 3 *inset*, left). Current was injected into the wide end of the electrode, and the voltage response at that point is the dotted line "cell with electrode (CE)". Subtracting C from CE gives the *effective* artefact ("CE – C", *dashed line*).

The extracellular artefact falls to below 5% of the cell alone response by 1.1 ms (i.e., 0.6 ms after the end of the pulse). The effective artefact, however, falls to less than 5% of the cell alone response only after 2.4 ms (i.e., 1.9 ms from the pulse end). This is about 3 times as long as the *recorded* artefact. (If the error tolerance is reduced from 5 to 2% of the cell alone response, the extracellular electrode artefact lasts 0.7 ms, and the effective artefact lasts 3.2 ms from the pulse end, a factor of 4.6 longer.)

The nonsumming cell-electrode interaction can be "dissected" into its waveform components with the nonuniform analytical solution. The components of the first three transients above are given in Table 7. The electrode behaves predominantly as a lumped resistor-capacitor circuit, with a time constant of 88 $\mu$s, just below the 113 $\mu$s one would predict from its resistance and capacitance. The faster component has a trivial amplitude by comparison with $A_0$. The amplitudes of even faster components (not shown) are progressively smaller. When the electrode is attached to the cell, the $\tau_0$ of the combined system is slightly slower than that of the cell alone, but the other time constants are remarkably similar to those of the cell alone, up to $n = 9$. However, $\tau_{10}$ is equal to 91 $\mu$s, which is different from the 82 $\mu$s $\tau_{10}$ of the cell but not far from the $\tau_0$ of the electrode (boxes for emphasis). At higher indices, $\tau_n$ of the combination corresponds closely to $\tau_{n-1}$ of the cell alone: it is as if the electrode time constant is inserted into the list, and faster cell time constants are moved along one to the right. This at least is consistent with a summing interaction. The same is not true, however, of the amplitudes: the large $A_0$ of the electrode is spread over many of the combined model's $A_n$ terms; $A_0$ is changed by 0.9%, $A_1$ by 1.5%, $A_2$ by 13.6%, and $A_3$ by 30%. The changes in $A_n$ become greater as $\tau_n$ approaches $\tau_0$ of the electrode alone, and then fall off again. The biggest component by far is $A_{10}$, the term corresponding to the electrode time constant, however its value of 68.6 mV is much reduced from the electrode-alone $A_0$ of 109.1 mV. Power has leaked out of the electrode term, and into neighboring cell terms, because of the coupling between the two structures. The effects of the $n = 2$ term can be expected to last for about three time constants, i.e., over 5 ms from the pulse end: whether this would make an important difference to the outcome of model fitting would require further simulations.

In other simulations, in which either the pipette capacitance or the pipette resistance was increased by a factor of only 1.25, the change in $A_0$ exceeded 1%, suggesting that in many experiments the effective artefact may be significant over the *entire duration* of the cell's response, and that it is an oversimplification to assert that the effective artefact is approximately 3 times the length of the extracellular control multiplied by the ratio of intracellular to extracellular electrode resistance (c.f. Paper III, Appendix). In such circumstances, particularly when electrode capacitance (after compensation) is large, it may be necessary to attach an explicit model of the electrode onto the model of the cell, fixing the capacitance and resistance to their measured values (e.g., Major et al., 1994).

The results above suggest that any uncompensated electrode capacitance must be treated with caution by modelers: its true effects may outlast the extracellular controls by a considerable factor and may affect optimal fit parameters, particularly $R_i$, which can be appreciably higher than its true value (see Major, 1992, Chapter 3). Early waveform components are boosted by increases in electrode resistance or decreases in capacitance neutralization (not shown). The duration of the extracellular control, the "fittability" of a cell's response, and the duration of the changes in the response when capacitance neutralization is reduced or electrode resistance alters can all act as rough guides to the earliest "safe" fit start time (see Major, 1992, chapters 3 and 6), or whether it might be necessary to model the electrode along with the

**TABLE 7 Nonsumming cell-electrode interaction**

| $n$ | 0 | 1 | 2 | 3 | 4 | 5 | 6 | 7 | 8 | 9 | 10 | 11 | 12 |
|---|---|---|---|---|---|---|---|---|---|---|---|---|---|
| Electrode alone* | | | | | | | | | | | | | |
| $\tau_n$ | 0.088 | 0.003 | | | | | | | | | | | |
| $A_n$ | 109.149 | 1.610 | | | | | | | | | | | |
| Cell alone† | | | | | | | | | | | | | |
| $\tau_n$ | 22.466 | 8.557 | 1.758 | 0.786 | 0.551 | 0.322 | 0.210 | 0.172 | 0.129 | 0.096 | 0.082 | 0.069 | 0.055 |
| $A_n$ | 1.033 | 0.453 | 0.059 | 1.573 | 0.844 | 0.001 | 0.411 | 0.762 | 0.029 | 0.059 | 0.447 | 0.062 | 0.003 |
| Cell with electrode* | | | | | | | | | | | | | |
| $\tau_n$ | 22.513 | 8.565 | 1.758 | 0.790 | 0.552 | 0.322 | 0.210 | 0.174 | 0.130 | 0.097 | 0.091 | 0.078 | 0.069 |
| $A_n$ | 1.042 | 0.460 | 0.067 | 2.049 | 1.190 | 0.002 | 1.373 | 3.214 | 0.292 | 11.507 | 68.610 | 22.710 | 1.177 |

Units: $\tau_n$, ms; $A_n$, mV.

† Injecting 1 nA × 0.5 ms short pulse into and recording from soma or wide end of electrode,* when present.

cell. More precise indications can be built up by detailed simulations of a particular experiment (e.g., Major et al., 1994).

## Example 4. Nonuniform CA1 pyramidal cell "cartoon" representation

To illustrate the nonuniform solutions with a more complex geometry showing branching, the cartoon representation (Stratford et al., 1989) of a real hippocampal CA1 pyramidal cell is employed. The physical dimensions of the representation are shown in Fig. 4 of Paper I, accompanying which there is a description of how it was obtained. Fig. 4 of the current paper shows the cartoon together with the $R_m$ and $R_i$ factors of its individual segments; $C_m$ is assumed to be uniform over the whole cell. The general trend is for $R_m$ to increase away from the soma (perhaps because of ions flooding out of a microelectrode), and to be lower in the apical than in the basal tree (for a possible justification see Major, 1992, chapter 5: there may be more conductances associated with "undershoot" after EPSPs in the apical dendrites; also see Nicoll et al., 1993). In addition, $R_i$ increases away from the soma (again, perhaps because of ionic concentration gradients resulting from the presence of a microelectrode, or perhaps because of increased cytoskeletal occlusion in thinner segments).

Three models are considered. All have the same biologically reasonable global electrical parameters: $C_m = 0.7$ $\mu$Fcm$^{-2}$, $R_m = 50{,}000$ $\Omega$cm$^2$, $R_i = 250$ $\Omega$cm, somatic $g_{shunt} = 10$ nS. The models differ in the magnitude and location of their single dendritic shunt. The default, "soma stab" model has no dendritic shunt. The "double stab" model has a 10-nS shunt at the distal end of segment 28, as if it had been impaled by a microelectrode (e.g., Wong and Stewart, 1992). This site is at the end of one of the twin apical trunks, about 360 $\mu$m from the soma, before the spine collapse procedure (see Paper I). The third model has a 1-nS shunt at the base of its single uncollapsed dendritic spine, at the end of segment 23 (assuming depth-first, left-first numbering, with the soma index 0).

The responses of the models are shown in Fig. 5, and their waveform components are listed up to $n = 9$ in Table 8. Two kinds of stimulus are used. In the upper two panels, a double exponential current (Eq. 51 of Paper I) with total charge 0.1 pC, $\tau_{sy_1} = 0.1$ ms and $\tau_{sy_2} = 2$ ms is injected into the spine head (see that paper for justification of current parameters). In Fig. 5 *C*, short current pulses of amplitude 1 nA and duration 0.5 ms are injected into the soma or the apical trunk impalement site (in the case of the double stab model).

Fig. 5 *A* shows the responses to synaptic input under "soma stab" and "double stab" conditions. The peak of the somatic PSP ("sp-s") is only decreased slightly by the extra dendritic conductance, and the final decay time constant is reduced from 18.9 to 15.1 ms. The fast time constants and amplitudes $A_{n_{26s}}$ ($n > 6$) are barely changed, and this is reflected in the close superposition of the two somatic responses at early times. Again, this is consistent with shunt effects only appearing at relatively late times in responses. The response at the dendritic recording site in the double stab model is also plotted ("sp-at"): it shows an earlier and bigger peak than the somatic response of the same model. The difference at early times is due partly to the longer distance (both physical and electrical) from the spine to the soma compared with the distance from the spine to the dendritic recording site, and partly due to "load effects": there are more side branches off the spine-to-soma route than off the route from the spine to

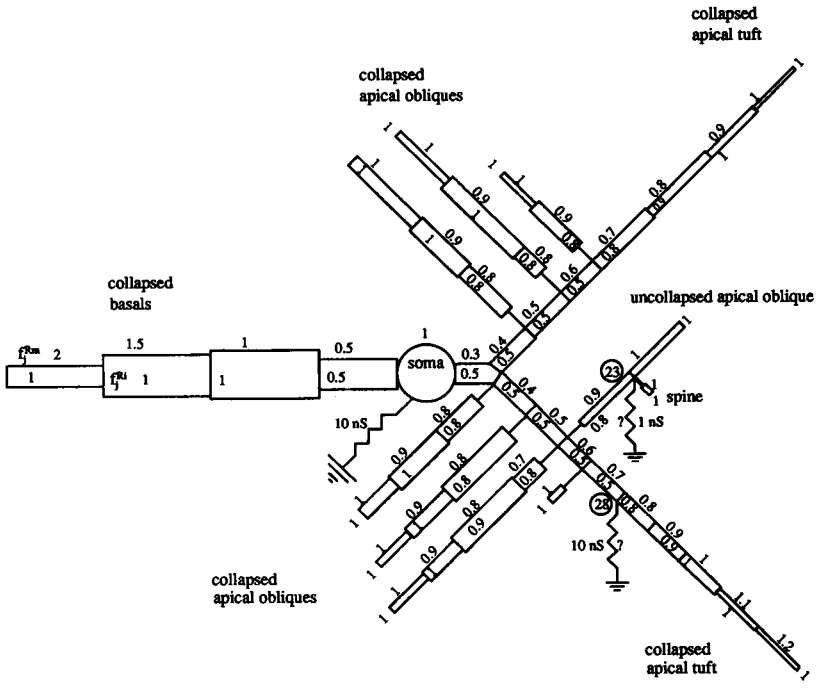


FIGURE 4 Cartoon Representation of hippocampal CA1 pyramidal cell from Paper I, Figs. 2 and 4. A nonuniform distribution of $R_m$ and $R_i$ is introduced: $f_j^{R_m}$ is written above each segment, and $f_j^{R_i}$ is written inside, just below, or just beside the end of each segment. See text for global electrical parameters. $f_j^{C_m} = 1$ for all segments. A left-first, depth-first numbering scheme for segments is assumed, with the soma having index 0. There is a 10-nS somatic shunt in all the models, to mimic the effects of impalement by a microelectrode. The default ("soma stab") model has no further shunts. The "double stab" model has an additional 10-nS shunt at the distal end of segment 28 (lower apical trunk). This has two interpretations: (i) a second electrode has impaled the apical dendrite, (ii) a strong, localized tonic shunting inhibition is being applied. A third model omits the apical trunk shunt, but has instead a 1-nS shunt at the base of the uncollapsed dendritic spine, at the distal end of segment 23. The resistors indicating the latter two shunts in the figure are labeled with question marks to emphasize that they are not present in all the models.

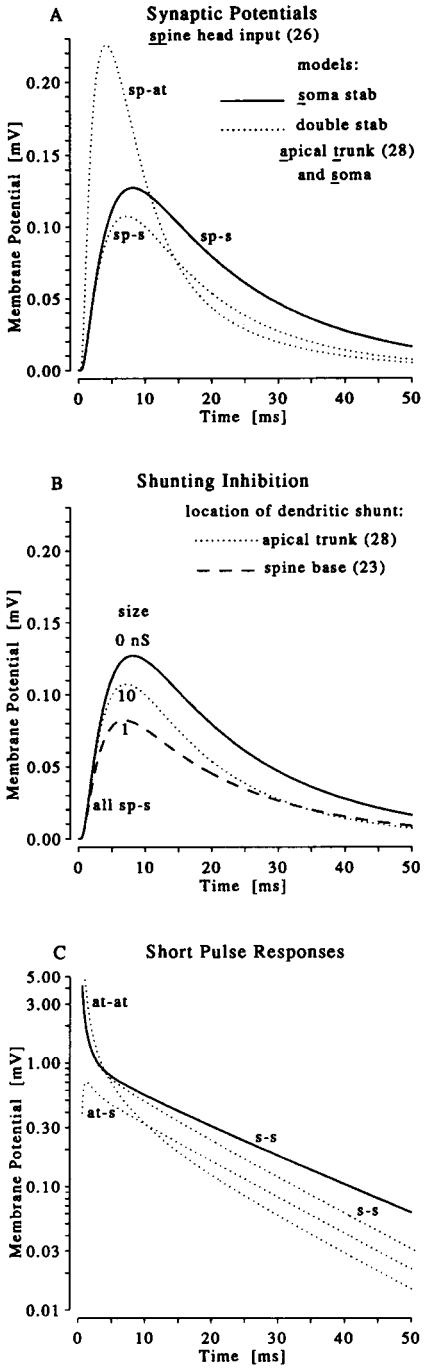


FIGURE 5 Responses of the cartoon models in Fig. 4. Solid lines: responses of default model (somatic shunt only). Dotted lines: responses of "double stab model", i.e., one with extra 10-nS shunt at distal end of segment 28 in one of the apical trunks. Dashed line: response of third model, with 1 nS shunt at spine base. Waveform labels of the form "e-r" indicate stimulation site e and recording site r, where "s" stands for "soma", "at" for "apical trunk" (distal end of segment 28), and "sp" for "spine head". Waveform components are listed in Table 8. The waveforms in the upper two panels are responses to a double exponential input current with total charge = 0.1 pC, $\tau_{sy_1}$ = 0.1 ms and $\tau_{sy_2}$ = 2 ms into the spine head (segment 26). (*A*) Somatic post synaptic potential (PSP) of default model (solid, "sp-s") compared with that of double stab model (dotted, "sp-s"). The response at the apical trunk "impalement" site in the double stab model is labeled "sp-at". (*B*) Illustration of shunting inhibition on input into the spine. All responses are recorded from the soma. Dotted line: response when a 10-nS localized "off-line" shunting inhibition is applied to the end of segment 28 (apical trunk). Dashed line: response when shunting inhibition of only 1 nS is applied "strategically" to the dendritic shaft just below the input site. (*C*) Responses to 1 nA × 0.5 ms short current pulses of "soma stab" and "double stab" models, logarithmic voltage axis. See text for discussion.

the dendritic recording site. The difference at late times is because, in relative terms, the dendritic shunt increases the local conductances to earth far more than the somatic shunt does, and so, loosely speaking, that part of the cell loses charge more rapidly than the soma. In fact, at late times charge flows from the soma towards the dendritic impalement site, so all parts of the cell discharge with the same final time constant. The differences in the final decays are in the amplitudes $A_{n_{26s}}$ and $A_{n_{26,28}}$.

Fig. 5 *B* is an illustration of how the nonuniform analytical solution can be used to explore shunting inhibition (e.g., Jack et al., 1975, chapter 7; Koch et al., 1990). The efficacy of a large "off-line" shunt is compared to that of a small "on-line" shunt, in their ability to depress the peak voltage at the soma in response to the synaptic stimulation outlined above. The "off-line" model is the same as the "double stab" model, merely being reinterpreted. The 10-nS shunt at the end of the lower apical trunk is not on the direct route between input spine and soma, and so has relatively little effect on the EPSP peak, although it causes a detectable (20%) change in $\tau_0$. The input resistance of the default ("soma stab") model is 43.1 MΩ, which is reduced to 36.5 MΩ by the 10-nS dendritic shunt, a 15% change, probably detectable under most conditions. By contrast, the more strategically placed 1-nS shunt at the base of the input spine has a much more pronounced effect on the peak EPSP, almost halving it. Inspection of Table 8 shows that the change in $\tau_0$ from the default model is less than 3%. The input resistance of the spine base shunting inhibition model is 42.4 MΩ, a reduction of less than 2% from the default model. Both changes would be hard to detect in experiments. Curiously, some of the faster time constants in this model ($\tau_4$–$\tau_6$), together with their associated amplitudes, appear to have changed more from the default model than have the equivalent ones in the double stab model, even though the latter has a bigger dendritic shunt. (We note that because $\tau_{sy2} \approx \tau_6$, the large opposite signed amplitudes of these two terms should be combined, leaving a net amplitude which is closer to the value in the default model.) This phenomenon should perhaps be explored in more detail.

Fig. 5 *C* compares the short pulse responses of the soma stab and double stab models, with a logarithmic voltage axis. The different final time constants of the two models are apparent. The two "s-s" or soma-soma responses are indistinguishable at early times, and their fast time constants and amplitudes largely agree to within two decimal places for $n > 6$. In terms of model fitting, the double stab model introduces one new parameter (dendritic $g_{shunt}$), assuming the impalement location is known. However, two additional waveforms, potentially, are available, the trunk-trunk response "at-at" and the trunk-soma transfer response "at-s", which because of reciprocity, should be the same as the soma-trunk transfer response (an additional

**TABLE 8 CA1 pyramidal cell cartoon models' response components**

| $n$ | 0 | 1 | 2 | 3 | 4 | 5 | 6 | 7 | 8 | 9 | $sy_2$ |
|---|---|---|---|---|---|---|---|---|---|---|---|
| Soma stab model | | | | | | | | | | | |
| $\tau_n$ | 18.86 | 6.99 | 5.39 | 4.01 | 3.26 | 2.97 | 2.58 | 1.76 | 1.61 | 1.45 | 2.0 |
| $A_{n26s}$ * | 0.23 | 0.05 | −0.07 | −0.01 | 0.06 | −0.06 | −0.62 | 0.01 | 0.04 | −0.01 | 0.34 |
| $A_{n_{ss}}$ † | 0.85 | 0.07 | 0.10 | 0.02 | 0.00 | 0.00 | 0.01 | 0.09 | 0.06 | 0.03 | |
| Double stab model | | | | | | | | | | | |
| $\tau_n$ | 15.07 | 6.80 | 5.08 | 4.01 | 3.17 | 2.96 | 2.52 | 1.76 | 1.61 | 1.45 | 2.0 |
| $A_{n_{26s}}$ * | 0.19 | 0.06 | −0.04 | −0.01 | 0.13 | −0.06 | −0.73 | 0.01 | 0.04 | −0.01 | 0.37 |
| $A_{n_{26,28}}$ * | 0.13 | 0.06 | 0.13 | 0.00 | 1.84 | 0.47 | −3.46 | 0.00 | 0.02 | 0.01 | 0.69 |
| $A_{n_{ss}}$ † | 0.84 | 0.14 | 0.04 | 0.02 | 0.00 | 0.00 | 0.02 | 0.09 | 0.06 | 0.02 | |
| $A_{n_{28,28}}$ † | 0.39 | 0.11 | 0.40 | 0.00 | 0.28 | 0.03 | 0.35 | 0.00 | 0.03 | 0.02 | |
| Spine base shunting inhibition model | | | | | | | | | | | |
| $\tau_n$ | 18.38 | 6.97 | 5.38 | 4.01 | 3.10 | 2.87 | 1.99 | 1.76 | 1.61 | 1.45 | 2.0 |
| $A_{n_{26s}}$ * | 0.13 | 0.03 | −0.03 | −0.00 | 0.04 | 0.04 | 21.91 | 0.03 | 0.07 | −0.01 | −22.24 |

Units: $\tau_n$; $A_{n_{er}}$, mV.

* Response to double exponential current, Q = 0.1 pC, into spine head.

† Response to 1 nA × 0.5 ms short current pulse.

test for linear behavior of the system). Both new responses contain valuable information. Because its $A_0$ and $A_2$ are of similar magnitude, the trunk-trunk response has a pronounced "slow bend," useful for constraining core electrotonic model nonuniqueness (see Major, 1992; Paper I; below): it should not be discarded. The transfer response has great potential for checking or further constraining a core electrotonic model. Compared with the other two responses, it should suffer less distortion at early times due to electrode artefacts. Therefore, assuming minimal or accurately quantified morphological errors, the transient transfer response should be well-suited to constrain the range of likely $R_i$ values. Ideally, in the time available experimentally, all three responses should be measured. Nonuniform model direct fit programs, such as the one described above, can then be used to obtain likely parameter ranges, given accurate morphological measurements and short pulse responses from the same cell, together with estimated relative $R_m$ and $R_i$ distribution functions.

## DISCUSSION

The solutions for transients in nonuniform branching cables presented above are extensions of those presented in Papers I and II of this series (Major et al., 1993a, b). Most of the general points discussed in those articles also apply to the nonuniform solution. The system (cell) time constants are independent of stimulation and recording sites and are obtained from a recursive transcendental equation. The amplitudes are composed of three factors, one constant over the whole cell, one varying with input site, and the other varying with recording site. All the convolutions detailed in Papers I and II hold for the nonuniform case. There is reciprocity between stimulus and recording site, for current injections. For voltage clamp, there is a further reciprocity relation: the clamp current resulting from a dendritic current injection is the same as the inverted voltage response at that point after a somatic voltage command, providing both inputs have the same time-course and magnitude (in appropriate units). The discussion in the Appendices of those two papers about lumped terms, efficacy, attenuation, A.C. responses, and singularity clashes can be generalized to the nonuniform case by using the Laplace transform response $\bar{G}$ described in the Appendices below. Singularity clashes can be avoided, as before, by small changes in the lengths of the involved segments. The parameter dependencies of the nonuniform and uniform solutions are similar (see Example 1).

As in the uniform case, for a given branching pattern, an infinite number of possible raw *electro-morphological* models map onto a particular core *electrotonic* model. All these models give the same response to a given stimulus, when input and recording sites are expressed as fractional distances along particular segments. A nonuniform raw electro-morphological model is specified by its physical *morphology* (branching pattern; $d_s$, $l_j$, $d_j$; for all segments $j$), distribution factors, global *specific* electrical parameters ($C_m$, $R_m$, $R_i$), and shunts. The corresponding core electrotonic model has a more compact mathematical representation, in terms of the same branching pattern and (for example) the parameter set $\{\tau_m, g_{sm}, g_{shunt}; \tau_{m_j}, L_j, g_{\infty_j}, g_{shunt_j}$, for all segments $j\}$. Alternative core parameterizations are possible, but all involve the $L_j$ terms, hence the name "electrotonic."

If the number of segments is $N$, and their branching pattern is fixed, there are $6N + 4$ raw electro-morphological parameters versus $4N + 3$ core electrotonic parameters for a nonuniform model. A uniform model has only $2N + 5$ raw versus $2N + 3$ core parameters (Paper I, p. 440; Evans et al., 1994). Compared with the uniform model, there are two extra core parameters per segment, namely $\tau_{m_j}$ and $g_{shunt_j}$, but there are four extra raw parameters: $f_j^{C_m}$, $f_j^{R_m}$, $f_j^{R_i}$ and $g_{shunt_j}$ (although one of the $f_j^{R_i}$ factors can be set equal to 1 without loss of generality, if global $R_i$ is set to that segment's $R_{i_j}$). More trade-offs between raw parameters are possible, therefore, in the nonuniform case for a given

core electrotonic model, because the distribution factors $f_j^{C_m}$, $f_j^{R_m}$ and $f_j^{R_i}$ can now be used to compensate for *localized* changes in physical dimensions without alterations to the global specific electrical parameters: the trade-offs in Paper I can now apply to individual segments as well as to entire cells.

In translating from an electro-morphological to a core electrotonic description, lengths and diameters are combined with (capacitance/unit area), (resistance of unit area), and (resistance of unit cross-sectional area/unit length), resulting in a more compact description in terms only of resistances, capacitances and dimensionless quantities (time constants can be thought of as having dimensions [resistance $\times$ capacitance]). As the number of parameters is reduced, information about *absolute* lengths and diameters is lost.

A similar raw-to-core mapping applies to compartmental models. For simplicity, suppose there are no shunts. The raw electro-morphological model, after multiplication of the global specific electrical parameters by the distribution factors, consists of the compartmentalised *morphology* and the local *specific* resistivities and capacitances. The core *electrical* model is the corresponding branching network of *actual* resistances and capacitances. A compartment in segment $j$ has five electro-morphological parameters (length, diameter, $R_{m_j}$, $C_{m_j}$, and $R_{i_j}$), but only three core electrical parameters (membrane resistance, membrane capacitance, and axial resistance). Various different combinations of raw parameters can therefore yield the same core model. Again, the absolute length and diameter information is lost.

Target data of insufficient quality will lead to core electrotonic model nonuniqueness, even when the distribution factors are known for a given type of cell. When the distribution factors are not known, a whole new world of nonuniqueness opens up (e.g., Rall et al., 1992). Fortunately, the errors arising from incorrect assumptions about $f_j^{R_m}$ may not be too serious if compensating shunts are allowed (see Example 2). These issues all need to be explored in more detail using models of real neurones.

It is worth emphasizing that errors in morphological measures will lead to errors in inferred values for specific electrical parameters such as $R_i$, even if the core electrotonic model is correct—irrespective of how it was obtained. Matching model responses from arbitrarily many different stimulation and recording sites with their experimental counterparts still allows only the *core electrotonic* model to be constrained. Translation of this back into a raw electro-morphological description, in order to deduce $C_{m_j}$, $R_{m_j}$, and $R_{i_j}$ in a particular segment, requires accurate morphological measurements of $l_j$ and $d_j$.

The power of the nonuniform solutions to explore issues such as nonsumming interactions between electrodes and cells is illustrated in Example 3. The effective artefact resulting from an electrode may be far worse than extracellular controls would suggest; indeed, it may be significant for the entire duration of a response. In such cases a nonuniform direct fitting program can be used to match a combined electrode-cell model to experimental data.

Shunting inhibition and dual or multiple recordings can also be explored using the nonuniform solutions (see Example 4), which can provide complementary insights to those obtained by conventional compartmental modelling techniques.

Tapering morphology or smooth spatial variations in the electrical parameters need to be approximated by step-wise changes, but for most purposes this should not prove to be a major deficiency. The most serious limitation of the solutions presented above is that they cannot deal with *transient conductances*: for these, compartmental models are still necessary. Despite the undoubted involvement of active conductances and synaptic conductance changes in the functioning of neurones, many important insights can be still obtained from passive cable modelling (e.g., Rall, 1977), and it is hoped that the nonuniform analytical solutions will prove to be a useful tool in this endeavor.

## APPENDICES

## Appendix 1: The amplitude terms using complex residues

We now derive the Laplace transform solution of the impulse response for arbitrarily branching geometry with a soma + shunt, nonuniform electrical parameters and dendritic shunts, and use it as in Bluman and Tuckwell (1987), Evans et al. (1992), and Paper I to derive the coefficients $A_{n_{er}}$.

### *Laplace transform of impulse response*

We define $G_r(X_r, Z_e, t)$ to be the spatially continuous voltage response at $X_r$ to a *unit* point charge at $Z_e$, (i.e., the solution to Eqs. 1–3, I.8–I.11 in segment $r$). At the soma it is defined to be $G_s$. Let $\bar{G}_j(X_j, Z_e, p)$ be the Laplace transform of $G_j(X_j, Z_e, t)$ with respect to a complex variable $p$. It satisfies the following problem: In each segment $j$ we have the ordinary differential equation,

$$\frac{d^2\bar{G}_j}{dX_j^2} - (\tau_{m_j}p + 1)\bar{G}_j = \begin{cases} -g_{\infty_e}^{-1}\delta(X_e - Z_e) & \text{if } j = e, \\ 0 & \text{otherwise,} \end{cases} \tag{16}$$

with boundary conditions:

at terminations

$$g_{\infty_j}\left(\frac{d\bar{G}_j}{dX_j}\right)_{X_j=L_j} + g_{\text{shunt}_j}(\bar{G}_j)_{X_j=L_j} = 0, \tag{17}$$

at branches

$$g_{\infty_p}\left(\frac{d\bar{G}_p}{dX_p}\right)_{X_p=L_p} + g_{\text{shunt}_p}(\bar{G}_p)_{X_p=L_p} = \sum_{d\in dtrs_p} g_{\infty_d}\left(\frac{d\bar{G}_d}{dX_d}\right)_{X_d=0}, \tag{18}$$

and Eqs. I.61 and I.62 at the soma. Integrating Eq. 16 across the input site $Z_e$ again gives us Eq. I.63.

### *Laplace transform solution*

Define

$$q_j \equiv (1 + \tau_{m_j}p)^{1/2}. \tag{19}$$

For all parent $p$ and daughter $d$ segments, we define

$$\bar{\mu}_p = \frac{1}{g_{\infty_p}q_p}\left[g_{\text{shunt}_p} + \sum_{d\in dtrs_p} g_{\infty_d}q_d\left(\frac{1 + \bar{\mu}_d\coth qL_d}{\coth qL_d + \bar{\mu}_d}\right)\right] \tag{20}$$

with

$$\bar{\mu}_j = \frac{g_{\text{shunt}_j}}{g_{\infty_j} q_j} \qquad \text{for all terminal segments } j. \tag{21}$$

Also, for all segments $j$,

$$\bar{\kappa}_j = \prod_{c \in chain_j} (\cosh q_c L_c + \bar{\mu}_c \sinh q_c L_c)^{-1}. \tag{22}$$

As in Paper I, we divide the dendritic tree into five zones, the solutions in which are given by Eqs. I.67–I.72 with $q$ being replaced by $q_j$ whenever it multiplies an electrotonic distance from segment $j$ (such as $L_j$, $X_j$, $(L_j - X_j)$, etc.). Following the same methods as in Paper I, it can be shown that

$$\bar{A}_s = \frac{\bar{\kappa}_e[\cosh q_e(L_e - Z_e) + \bar{\mu}_e \sinh q_e(L_e - Z_e)]}{g_s[1 + \tau_s p] + \sum_{st \in stems} g_{\infty_{st}} q_{st} \bar{\kappa}_{st} (\sinh q_{st} L_{st} + \bar{\mu}_{st} \cosh q_{st} L_{st})}, \tag{23}$$

and for parent $p$ and daughter $c$ on the "mainline" soma-input chain,

$$\begin{aligned} \bar{B}_c = {} & g_{\infty_p} q_p (\cosh q_p L_p + \bar{\mu}_p \sinh q_p L_p) \\ & \times (\cosh q_c L_c + \bar{\mu}_c \sinh q_c L_c) \bar{B}_p / g_{\infty_c} q_c, \end{aligned} \tag{24}$$

where for the chain's stem segment $st$

$$\bar{B}_{st} = \frac{\bar{\kappa}_e[\cosh q_e(L_e - Z_e) + \bar{\mu}_e \sinh q_e(L_e - Z_e)]}{\bar{\kappa}_{st} q_{st} g_{\infty_{st}}}, \tag{25}$$

and $\bar{B}_e$ is given by Eq. I.74 with $q_e$ replacing $q$.

### *Obtaining $A_{n_{er}}$ by complex residues*

In cases where there are no singularity coincidences in the transcendental equation (Eq. 11), the amplitude terms may be determined by evaluating the residue of $\tilde{G}_r(X_r, Z_e, p)$ at the simple pole $p = -1/\tau_n$, i.e., at $q_j = i\alpha_{jn}$ (see Paper I and Priestley, 1985, p. 110). Thus,

$$A_{n_{er}} = \lim_{p \to -1/\tau_n} (p + 1/\tau_n) \tilde{G}_r(X_r, Z_e, p) = \left. \frac{h(p)}{k'(p)} \right|_{p = -1/\tau_n}, \tag{26}$$

where

$$\begin{aligned} h(p) = {} & \bar{\kappa}_e \bar{\kappa}_r [\cosh q_e(L_e - Z_e) + \bar{\mu}_e \sinh q_e(L_e - Z_e)] \\ & \times [\cosh q_r(L_r - X_r) + \bar{\mu}_r \sinh q_r(L_r - X_r)] \end{aligned} \tag{27}$$

and

$$k(p) = g_s(1 + \tau_s p) + \sum_{st \in stems} q_{st} g_{\infty_{st}} \bar{\kappa}_{st} (\sinh q_{st} L_{st} + \bar{\mu}_{st} \cosh q_{st} L_{st}). \tag{28}$$

It can be shown, using $dq_j/dp = \tau_{m_j}/2q_j$, that

$$k'(p) = g_s \tau_s + \frac{1}{2} \sum_{st \in stems} \tau_{m_{st}} g_{\infty_{st}} \bar{\kappa}_{st}^2 \left\{ \frac{(1 + \bar{\mu}_{st}^2) \sinh 2q_{st} L_{st} + 4 \bar{\mu}_{st} \sinh^2 q_{st} L_{st}}{2q_{st}} + L_{st}(1 - {}^2_{st}) + \left\langle \frac{d\bar{\mu}_{st}}{dq_{st}} + \frac{\bar{\mu}_{st}}{q_{st}} \right\rangle \right\}, \tag{29}$$

and, using $dq_d/dq_p = q_p \tau_{m_d}/q_d \tau_{m_p}$, that

$$\begin{aligned} & \frac{d\bar{\mu}_p}{dq_p} + \frac{\bar{\mu}_p}{q_p} \\ & = \frac{1}{\tau_{m_p} g_{\infty_p} \bar{\kappa}_p^2} \sum_{d \in dtrs_p} g_{\infty_d} \tau_{m_d} \bar{\kappa}_d^2 \left\{ \frac{(1 + \bar{\mu}_d^2) \sinh 2q_d L_d + 4\bar{\mu}_d \sinh^2 q_d L_d}{2q_d} + L_d(1 - \bar{\mu}_d^2) + \left\langle \frac{d\bar{\mu}_d}{dq_d} + \frac{\bar{\mu}_d}{q_d} \right\rangle \right\}, \end{aligned} \tag{30}$$

with

$$\frac{d\bar{\mu}_j}{dq_j} = -\frac{\bar{\mu}_j}{q_j}, \tag{31}$$

at tip segments $j$. Starting from Eq. 29, recursively expanding terms marked by $\langle \square \rangle$ using Eq. 30 until the tip segments are reached, it can be shown that

$$k'(p) = g_s \tau_s + \frac{1}{2} \sum_{j \in segs} \tau_{m_j} g_{\infty_j} \bar{\kappa}_j^2 \left\{ \frac{(1 + \bar{\mu}_j^2) \sinh 2q_j L_j + 4\bar{\mu}_j \sinh^2 q_j L_j}{2q_j} + L_j(1 - \bar{\mu}_j^2) \right\}. \tag{32}$$

Using Eqs. 27, 32 and I.88 in Eq. 26 gives the expression for $A_{n_{er}}$ in Eqs. 4, 13, and 14.

## Appendix 2: Amplitude terms for perfect voltage clamp

We follow the working above and in Paper II, Appendix 1, with differences highlighted.

### *Case I: Clamp to zero with synaptic input: $V_{com} = 0$ and unit dendritic point charge*

The Laplace transform of the system of equations describing the model is the same as Eqs. 16–18, with Eq. II.63 at the soma. Eqs. II.64 and II.65 still hold, as do the definitions of $\bar{\mu}_p$ and $\bar{\kappa}_j$ above (Eqs. 20–22). We use the same representation scheme for $\tilde{G}_j$ as in Appendix 1. As explained in Paper II, $\bar{B}_{st}$ comes to dominate $\tilde{G}$ near its poles at $q_j = i\alpha_{jn}$, as the other $\bar{B}_c$ terms tend to zero. We define

$$\begin{aligned} h(p) = {} & \frac{\bar{\kappa}_e \bar{\kappa}_r}{\bar{\kappa}_{st}^2 q_{st}} [\cosh q_e(L_e - Z_e) + \bar{\mu}_e \sinh q_e(L_e - Z_e)][\cosh q_r(L_r - Z_r) \\ & + \bar{\mu}_r \sinh q_r(L_r - X_r)] \end{aligned} \tag{33}$$

when $r \neq st$ and

$$h(p) = \frac{\bar{\kappa}_e[\cosh q_e(L_e - Z_e) + \bar{\mu}_e \sinh q_e(L_e - Z_e)] \sinh q_{st} X_{st}}{\bar{\kappa}_{st} q_{st} \sinh q_{st} L_{st}} \tag{34}$$

when $r = st$, with

$$k(p) = g_{\infty_{st}} (\bar{\kappa}_{st} \sinh q_{st} L_{st})^{-1} = g_{\infty_{st}} [\coth q_{st} L_{st} + \bar{\mu}_{st}]. \tag{35}$$

Evaluating the residues at the simple poles $p = -1/\tau_n$, we have

$$k'(p) = \frac{\tau_{m_{st}}}{2q_{st}} g_{\infty_{st}} \left\{ L_{st}(1 - \coth^2 q_{st} L_{st}) \frac{\bar{\mu}_{st}}{q_{st}} + \left\langle \frac{d\bar{\mu}_{st}}{dq_{st}} + \frac{\bar{\mu}_{st}}{q_{st}} \right\rangle \right\}. \tag{36}$$

The recursive expansion Eq. 30 can be used in Eq. 36, and when evaluated with $h(p)$ in Eqs. 33 and II.6 gives $E_{n_{st}}$ in Eq. 15.

### *Case II: Unit voltage impulse command: $V_{com} = \delta(t)$, no dendritic inputs*

The derivation is as in Paper II, with $k(p)$ as in Eq. 35 and with $h(p)$ given by

$$h(p) = g_{\infty_{st}} \frac{\bar{\kappa}_r}{\bar{\kappa}_{st}} \frac{[\cosh q_r(L_r - Z_r) + \bar{\mu}_r \sinh q_r(L_r - Z_r)]}{\sinh q_{st} L_{st}}. \tag{37}$$

G. Major is currently a Wellcome Mathematical Biology Training Fellow. J. D. Evans has been funded on a Wellcome Trust program grant. We would like to thank the Wellcome Trust for funding the SUN computer system, John Clements and Steve Redman for the use of a now mutated

compartmental modeling package, Dennis Noble, Dave Attwell, Guy Kember, Alan Larkman, and Ken Stratford for helpful discussions, and Julian Jack for his many vital suggestions and for acting as "Godfather" to the whole project.

## REFERENCES


Barrett, J. N., and W. E. Crill. 1974. Specific membrane properties of cat motoneurones. *J. Physiol.* 239:301–324.

Bluman, G. W., and H. C. Tuckwell. 1987. Techniques for obtaining analytical solutions for Rall's model neuron. *J. Neurosci. Methods* 20: 151–166.

Churchill, R. V. 1942. Expansions in series of non-orthogonal functions. *Am. Math. Soc. Bull.* 48:143–149.

Clegg, J. S. 1984a. Properties and metabolism of the aqueous cytoplasm and its boundaries. *Am. J. Physiol.* 246:R133–R151.

Clegg, J. S. 1984b. Intracellular water and the cytomatrix: some methods of study and current views. *J. Cell. Biol.* 99:167s–171s.

Clements, J. D., and S. J. Redman. 1989. Cable properties of cat spinal motoneurons measured by combining voltage clamp, current clamp and intracellular staining. *J. Physiol.* 409:63–87.

Clements, J. D. 1986. Ph.D. dissertation. Australian National University, Canberra, Australia.

Douglas, R. J., and K. A. C. Martin. 1992. Exploring cortical microcircuits: a combined anatomical, physiological, and computational approach. *In* Single Neuron Computation. T. McKenna, J. Davis, and S. F. Zornetzer, editors. Academic Press, San Diego, CA. 381–412.

Ellisman, M. H., and S. R. Levinson. 1982. Immunocytochemical localization of sodium channel distributions in the excitable membranes of *Electrophorus electricus*. *Proc. Natl. Acad. Sci. USA.* 79:6707–6711.

Evans, J. D., G. C. Kember, and G. Major. 1992. Techniques for obtaining analytical solutions to the multi-cylinder somatic shunt cable model for passive neurones. *Biophys. J.* 63:350–365.

Evans, J. D., G. C. Kember, and G. Major. 1994. Techniques for the application of the analytical solution to the multi-cylinder somatic shunt cable model for passive neurones. *Math. Biosci.* In press.

Fleshman, J. W., I. Segev, and R. E. Burke. 1988. Electrotonic architecture of type-identified $\alpha$-motoneurons in the cat spinal cord. *J. Neurophysiol.* 60:60–85.

Fromherz, P., and T. Vetter. 1992. Cable properties of arborized Retzius cells of the leech in culture as probed by a voltage-sensitive dye. *Proc. Natl. Acad. Sci. USA.* 89:2041–2045.

Hillman, D., S. Chen, T. T. Aung, B. Cherksey, M. Sugimori, and R. R. Llinás. 1991. Localization of P-type calcium channels in the central nervous system. *Proc. Natl. Acad. Sci. USA.* 88:7076–7080.

Hines, M. 1984. Efficient computation of branched nerve equations. *Int. J. Biomed. Comput.* 15:69–76.

Hines, M. 1989. A program for simulation of nerve equations with branching geometries. *Int. J. Biomed. Comput.* 24:55–68.

Hodgkin, A. L., and A. F. Huxley. 1952. A quantitative description of membrane current and its application to conduction and excitation in nerve. *J. Physiol.* 117:500–544.

Holmes, W. R. 1986. A continuous cable method for determining the transient potential in passive dendritic trees of known geometry. *Biol. Cybern.* 55:115–124.

Holmes, W. R., I. Segev, and W. Rall. 1992. Interpretation of time constant and electrotonic length estimates in multicylinder or branched neuronal structures. *J. Neurophysiol.* 68:1401–1420.

Holmes, W. R., and C. D. Woody. 1989. Effects of uniform and non-uniform synaptic 'activation distributions' on the cable properties of modeled cortical pyramidal neurons. *Brain Res.* 505:12–22.

Hounsgaard, J., and J. Midtgaard. 1989. Dendrite processing in more ways than one. *Trends Neurosci.* 12:313–315.

Huguenard, J. R., O. P. Hamill, and D. A. Prince. 1989. Sodium channels in dendrites of rat cortical pyramidal neurons. *Proc. Natl. Acad. Sci. USA.* 86:2473–2477.

Jack, J. J. B., D. Noble, and R. W. Tsien. 1975. Electric Current Flow in Excitable Cells. Oxford: Oxford University Press, Oxford, UK. 502 pp.

Jaffe, D. B., D. Johnston, N. Lasser-Ross, J. E. Lisman, H. Miyakawa, and W. N. Ross. 1992. The spread of $Na^+$ spikes determines the pattern of dendritic $Ca^{2+}$ entry into hippocampal neurons. *Nature.* 357: 244–246.

Jonas, P., G. Major, and B. Sakmann. 1993. Quantal components of unitary EPSCs at the mossy fibre synapse on CA3 pyramidal cells of rat hippocampus. *J. Physiol.* 472:615–663.

Koch, C., R. Douglas, and U. Wehmeier. 1990. Visibility of synaptically induced conductance changes: theory and simulations of anatomically characterized cortical pyramidal cells. *J. Neurosci.* 10:1728–1744.

Koch, C., and T. Poggio. 1985. The synaptic veto mechanism: does it underlie direction and orientation selectivity in the visual cortex? *In* Models of the visual cortex. D. R. Rose and V. G. Dobson, editors. Wiley, New York. 408–419.

Larkman, A. U. 1991. Dendritic morphology of pyramidal neurones of the visual cortex of the rat: III. Spine Distributions. *J. Comp. Neurol.* 306: 332–343.

Larkman, A. U., G. Major, K. J. Stratford, and J. J. B. Jack. 1992. Dendritic morphology of pyramidal neurones of the visual cortex of the rat: IV. Electrical Geometry. *J. Comp. Neurol.* 323:153–166.

Llinás, R. R. 1988. The intrinsic electrophysiological properties of mammalian neurons: insights into central nervous system function. *Science.* 242:1654–1664.

Major, G. 1992. The Physiology, Morphology and Modelling of Cortical Pyramidal Neurones. D. Phil. thesis. Oxford University, Oxford, UK. 275 pp.

Major, G. 1993. Solutions for transients in arbitrarily branching cables: III. voltage clamp problems. *Biophys. J.* 65:469–491.

Major, G., J. D. Evans, and J. J. B. Jack. 1993a. Solutions for transients in arbitrarily branching cables: I. voltage recording with a somatic shunt. *Biophys. J.* 65:423–449.

Major, G., J. D. Evans, and J. J. B. Jack. 1993b. Solutions for transients in arbitrarily branching cables: II. voltage clamp theory. *Biophys. J.* 65: 450–468.

Major, G., A. U. Larkman, P. Jonas, B. Sakmann, and J. J. B. Jack. 1994. Detailed passive cable models of whole-cell recorded CA3 pyramidal neurones in rat hippocampal slices. *J. Neurosci.* In press.

Nelder, J. A., and R. Mead. 1965. A geometric technique for optimisation. *Computer J.* 7:308–327.

Nicoll, A., A. Larkman, and C. Blakemore. 1993. Modulation of EPSP shape and efficacy by intrinsic membrane conductances in rat neocortical pyramidal neurons *in vitro*. *J. Physiol.* 468:693–710.

Perkel, D. H., B. Mulloney, and R. W. Budelli. 1981. Quantitative methods for predicting neuronal behaviour. *Neuroscience.* 6:823–837.

Press, W. H., B. P. Flannery, S. A. Teukolsky, and W. T. Vetterling. 1988. Numerical Recipes in C: The Art of Scientific Computing. Cambridge University Press, Cambridge, UK. 735 pp.

Priestley, H. A. 1985. Introduction to Complex Analysis. Oxford University Press, Oxford, UK. Chapter 7.

Purves, R. D. 1981. Microelectrode Methods for Intracellular Recording and Ionophoresis. Academic Press, London, UK. 146 pp.

Rall, W. 1962. Theory of physiological properties of dendrites. *Ann. N. Y. Acad. Sci.* 96:1071–1092.

Rall, W. 1964. Theoretical significance of dendritic trees for neuronal input-output relations. *In* Neural theory and modelling. R.F. Reiss, editor. Stanford University Press, Stanford, CA. 73–97.

Rall, W. 1969. Time constants and electrotonic length of membrane cylinders and neurons. *Biophys. J.* 9:1483–1508.

Rall, W. 1977. Core conductor theory and cable properties of neurons. *In* Handbook of Physiology. The Nervous System. Cellular Biology of Neurones. E. R. Kandel, editor. American Physiological Society, Bethesda, MD. Sect. 1, Vol. 1, Part 1. 39–98.

Rall, W., R. E. Burke, W. R. Holmes, J. J. B. Jack, S. J. Redman, and I. Segev. 1992. Matching dendritic neuron models to experimental data. *Physiol. Rev.* 72:S159–S186.

Rapp, M., Y. Yarom, and I. Segev. 1992. The impact of parallel fiber background activity on the cable properties of cerebellar purkinje cells. *Neural Computation.* 4:518–533.

Shelton, D. P. 1985. Membrane resistivity estimated for the Purkinje neuron by means of a passive computer model. *Neurosci.* 14:111–131.

Stevens, J. K., J. Trogadis, and J. R. Jacobs. 1988. Development and control of axial neurite form: a serial electron microscopic analysis. *In* Intrinsic

determinants of neuronal form and function. R. J. Lasek and M. M. Black, editors. Alan R. Liss, New York. 115–145.

Stratford, K. J., A. J. R. Mason, A. U. Larkman, G. Major, and J. J. B. Jack. 1989. The modelling of pyramidal neurones in the visual cortex. *In* The Computing Neurone. R. Durbin, C. Miall, and G. Mitchison, editors. Addison-Wesley, Reading, UK. 296–321.

Stuart, G. J., H.-U. Dodt, and B. Sakmann. 1993. Patch-clamp recordings from the soma and dendrites of neurons in brain slices using infrared video microscopy. *Pflügers Arch.* 423:511–518.

Takashima, S. 1976. Membrane capacity of squid giant axon during hyper- and depolarisations. *J. Membrane Biol.* 27:21–39.

Thurbon, D., A. Field, and S. J. Redman. 1994. Electrotonic profiles of interneurones in stratum pyramidale of the CA1 region of rat hippocampus. *J. Neurophysiol.*, In press.

Trimmer, J. S. 1991. Immunological identification and characterisation of a delayed rectifier $K^+$ channel polypeptide in rat brain. *Proc. Natl. Acad. Sci. USA.* 88:10764–10768.

Westenbroek, R. E., M. K. Ahlijanian, and W. A. Catterall. 1990. Clustering of L-type $Ca^{2+}$ channels at the base of major dendrites in hippocampal pyramidal neurones. *Nature.* 347:281–284.

Westenbroek, R. E., J. W. Hell, C. Warner, S. J. Dubel, T. P. Snutch, and W. A. Catterall. 1992. Biochemical properties and subcellular distribution of an N-type calcium channel $\alpha 1$ subunit. *Neuron.* 9:1099–1115.

Wilson, C. J. 1984. Passive cable properties of dendritic spines and spiny neurons. *J. Neurosci.* 4:281–297.

Wilson, M. A., and J. M. Bower. 1989. The simulation of large-scale neural networks. *In* Methods in Neuronal Modelling. C. Koch, and I. Segev, editors. M. I. T. Press, Cambridge, MA. 291–333.

Wong, R. K. S., and M. Stewart. 1992. Different firing patterns generated in dendrites and somata of CA1 pyramidal neurones in guinea-pig hippocampus. *J. Physiol.* 457:675–687.